Boinepalli, Sharada; Leinweber, Derek Bruce; Moran, Peter John; Williams, Anthony Gordon; Zanotti, James Michael; Zhang, Jian-Bo
Electromagnetic structure of decuplet baryons towards the chiral regime Physical Review D, 2009; 80(5):054505

http://link.aps.org/doi/10.1103/PhysRevD.80.054505

PHYSICAL REVIEW D **80,** 054505 (2009)

Electromagnetic structure of decuplet baryons towards the chiral regime

S. Boinepalli,[1] D. B. Leinweber,[1] P. J. Moran,[1] A. G. Williams,[1] J. M. Zanotti,[2] and J. B. Zhang[3]
[1]*Department of Physics and Mathematical Physics and Special Research Centre for the Subatomic Structure of Matter, University of Adelaide, 5005, Australia*
[2]*School of Physics and Astronomy, University of Edinburgh, Edinburgh EH9 3JZ, United Kingdom*
[3]*Department of Physics, Zhejiang University, Hangzhou, Zhejiang 310027, People's Republic of China*
(Received 23 February 2009; published 22 September 2009)

The electromagnetic properties of the baryon decuplet are calculated in quenched QCD on a $20^3 \times 40$ lattice with a lattice spacing of 0.128 fm using the fat-link irrelevant clover fermion action with quark masses providing a pion mass as low as 300 MeV. Magnetic moments and charge radii are extracted from the electric and magnetic form factors for each individual quark sector. From these, the corresponding baryon properties are constructed. We present results for the higher-order moments of the spin-3/2 baryons, including the electric-quadrupole moment $E2$ and the magnetic-octupole moment $M3$. The world's first determination of a nonzero $M3$ form factor for the Δ baryon is presented. With these results we provide a conclusive analysis which shows that decuplet baryons are deformed. We compare the decuplet-baryon results from a similar lattice calculation of the octet baryons. We establish that the environment sensitivity is far less pronounced for the decuplet baryons compared to the octet baryons. A surprising result is that the charge radii of the decuplet baryons are generally smaller than those of the octet baryons. The magnetic moment of the Δ^+ reveals a turnover in the low quark-mass region, making it smaller than the proton magnetic moment. These results are consistent with the expectations of quenched chiral perturbation theory. A similar turnover is also noticed in the magnetic moment of the Σ^{*0}, but not for Ξ^* where only kaon loops can appear in quenched QCD. The electric-quadrupole moment of the Ω^- baryon is positive when the negative charge factor is included, and is equal to $0.86 \pm 0.12 \times 10^{-2}$ fm^2, indicating an oblate shape.

DOI: 10.1103/PhysRevD.80.054505 PACS numbers: 12.38.Gc, 12.39.Fe, 13.40.Em, 14.20.Dh

I. INTRODUCTION

The study of the electromagnetic properties of baryons provides valuable insight into the nonperturbative structure of QCD (see Refs. [1–5] for recent reviews). Baryon charge radii and magnetic moments provide an excellent opportunity to observe the nonanalytic behavior predicted by chiral effective field theory (χEFT). Since these are inherently nonperturbative properties of hadrons, first-principles calculations on the lattice are essential for our understanding of hadronic structure, and indeed there has been much progress in this direction, mainly for the nucleon and pseudoscalar states (see [6] for a review). For decuplet baryons, however, there has been very little progress since Ref. [7] which appeared almost 15 years ago. However, renewed interest appeared recently [8,9].

The Adelaide group has been investigating the electromagnetic structure of hadrons for several years now. In Refs. [10,11], we presented a novel method for determining the strange quark contribution to the nucleon's electromagnetic form factors, the results of which were later confirmed by an improved analysis of old experimental data [12] and new data from parity violating experiments at JLab [13]. This was followed by an in-depth study in quenched QCD of the electromagnetic properties of the octet baryons [14]. Of particular interest was an observed environmental isospin dependence of the strange quark distributions in Λ^0 and Σ^0. More recently, we performed an investigation into the pseudoscalar and vector meson electromagnetic form factors [15]. Here we determined that the ρ^+ meson has a negative quadrupole moment, indicating that the ρ meson is oblate.

In this paper we continue our study of the electromagnetic structure of hadrons and present a quenched lattice QCD calculation of the electromagnetic form factors of $SU(3)_{\text{flavor}}$ decuplet baryons. From these form factors we determine magnetic moments and charge radii, and also present results for the electric-quadrupole and magnetic-octupole moments.

On the lattice, decuplet baryons are stable as a result of the unphysical large quark masses that are used in present calculations and the finite volume of the lattice. Decay to a pion and an octet baryon is forbidden by energy conservation. However, stability of decuplet baryons is common to most hadronic models. In this sense, lattice results provide a useful forum in which the strengths and weaknesses of various models may be identified. The lattice results also provide access to observables not readily available with present experiments such as the higher-order multipole moments of the Ω^-, which is stable to strong interactions.

An examination of decuplet-baryon structure in lattice QCD enables one to study new aspects of nonperturbative quark-gluon dynamics. In analyzing the results we make comparisons within the baryon decuplet and with the octet results [14] which provide insights into the spin dependence of quark interactions.

The $E2$ and $M3$ moments accessible in spin-$3/2$ systems provide insights into the shape of the decuplet-baryon ground state. These higher-order moments also have the potential to discriminate among various model descriptions of hadronic phenomena.

To put our results into perspective, we compare our calculations with experimental measurements where available, and with the predictions of quenched chiral perturbation theory (QχPT).

The decuplet-baryon interpolating fields used in the correlation functions are discussed in Sec. II A. The extraction of baryon mass and electromagnetic form factors proceeds through a calculation of two- and three-point correlation functions. These are discussed in Sec. II B. The two- and three-point functions for decuplet baryons are discussed in Secs. II C and II D. Throughout this analysis we employ the lattice techniques introduced in [7], and these are summarized in Sec. III. In Sec. IV we outline the methods used in our analysis of the lattice two- and three-point functions. Our results are presented and discussed in Sec. V, and summarized in Sec. VI.

II. THEORETICAL FORMALISM

A. Interpolating fields

The commonly used interpolating field for exciting the Δ^{++} resonance from the QCD vacuum takes the long established [16,17] form of

$$\chi_\mu^{\Delta^{++}}(x) = \epsilon^{abc}(u^{Ta}(x)C\gamma_\mu u^b(x))u^c(x). \tag{2.1}$$

Unless otherwise noted, we follow the notation of Sakurai [18]. The Dirac gamma matrices are Hermitian and satisfy $\{\gamma_\mu, \gamma_\nu\} = 2\delta_{\mu\nu}$, with $\sigma_{\mu\nu} = \frac{1}{2i}[\gamma_\mu, \gamma_\nu]$. $C = \gamma_4\gamma_2$ is the charge conjugation matrix, a, b, and c are color indices, $u(x)$ is a u-quark field, and the superscript T denotes transpose. The generalization of this interpolating field for the Δ^+ composed of two u quarks and one d quark has the form

$$\chi_\mu^{\Delta^+}(x) = \frac{1}{\sqrt{3}}\epsilon^{abc}[2(u^{Ta}(x)C\gamma_\mu d^b(x))u^c(x) + (u^{Ta}(x)C\gamma_\mu u^b(x))d^c(x)]. \tag{2.2}$$

Other decuplet-baryon interpolating fields are obtained with the appropriate substitutions of $u(x), d(x) \to u(x), d(x)$ or $s(x)$. The interpolating field for Σ^{*0} is given by the symmetric generalization

$$\chi_\mu^{\Sigma^{*0}}(x) = \sqrt{\frac{2}{3}}\epsilon^{abc}[(u^{Ta}(x)C\gamma_\mu d^b(x))s^c(x) + (d^{Ta}(x)C\gamma_\mu s^b(x))u^c(x) + (s^{Ta}(x)C\gamma_\mu u^b(x))d^c(x)]. \tag{2.3}$$

The $SU(2)$-isospin symmetry relationship for Σ^* form factors

$$\Sigma^{*0} = \frac{\Sigma^{*+} + \Sigma^{*-}}{2} \tag{2.4}$$

may be easily seen in the Σ^{*0} interpolating field by noting

$$\epsilon^{abc}(s^{Ta}(x)C\gamma_\mu u^b(x))d^c(x) = \epsilon^{abc}(u^{Ta}(x)C\gamma_\mu s^b(x))d^c(x). \tag{2.5}$$

B. Correlation functions

Two-point correlation functions at the quark level are obtained through the standard procedure of contracting pairs of quark fields. Considering the Δ^+ correlation function at the quark level and performing all possible quark field contractions gives the two-point function as

$$\begin{aligned}\langle T(\chi_\mu^{\Delta^+}(x)\bar{\chi}_\nu^{\Delta^+}(0))\rangle = \tfrac{1}{3}\epsilon^{abc}\epsilon^{a'b'c'}\{&4S_u^{aa'}\gamma_\nu C S_u^{Tbb'}C\gamma_\mu S_d^{cc'}\\ &+ 4S_u^{aa'}\gamma_\nu C S_d^{Tbb'}C\gamma_\mu S_u^{cc'}\\ &+ 4S_d^{aa'}\gamma_\nu C S_u^{Tbb'}C\gamma_\mu S_u^{cc'}\\ &+ 2S_u^{aa'}\,\mathrm{tr}[\gamma_\nu C S_u^{Tbb'}C\gamma_\mu S_d^{cc'}]\\ &+ 2S_u^{aa'}\,\mathrm{tr}[\gamma_\nu C S_d^{Tbb'}C\gamma_\mu S_u^{cc'}]\\ &+ 2S_d^{aa'}\,\mathrm{tr}[\gamma_\nu C S_u^{Tbb'}C\gamma_\mu S_u^{cc'}]\},\end{aligned} \tag{2.6}$$

where the quark propagator $S_u^{aa'} = T(u^a(x)\bar{u}^{a'}(0))$ and similarly for the other quark flavors. $SU(3)_{\mathrm{flavor}}$ symmetry is clearly displayed in this equation.

In determining the three-point function, one encounters two topologically different ways of performing the current insertion. Figure 1 displays skeleton diagrams for these two insertions. These diagrams may be dressed with an arbitrary number of gluons. Diagram (a) illustrates the connected insertion of the current to one of the valence quarks of the baryon. Diagram (b) accounts for the alternative time ordering where the current first produces a disconnected $q\bar{q}$ pair which in turn interacts with the valence quarks of the baryon via gluons.

The number of terms in the three-point function is 4 times that in Eq. (2.6). The correlation function relevant for a Δ^+ three-point function is

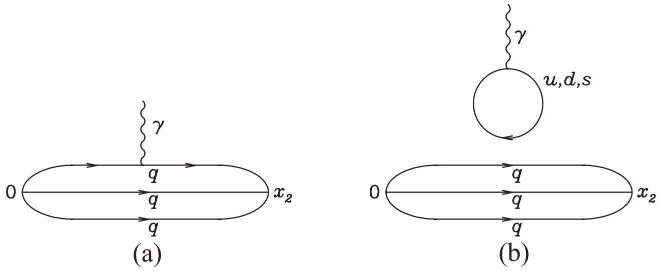

(a) (b)

FIG. 1. Diagrams illustrating the two topologically different insertions of the current within the framework of lattice QCD.

$$\begin{aligned} T(\chi_\mu^{\Delta^+}(x_2) j^\alpha(x_1) \bar{\chi}_\nu^{\Delta^+}(0)) = {} & \frac{1}{3} \epsilon^{abc} \epsilon^{a'b'c'} \{ 4\hat{S}_u^{aa'} \gamma_\nu C S_u^{Tbb'} C \gamma_\mu S_d^{cc'} + 4\hat{S}_u^{aa'} \gamma_\nu C S_d^{Tbb'} C \gamma_\mu S_u^{cc'} + 4\hat{S}_d^{aa'} \gamma_\nu C S_u^{Tbb'} C \gamma_\mu S_u^{cc'} \\ & + 4S_u^{aa'} \gamma_\nu C \hat{S}_u^{Tbb'} C \gamma_\mu S_d^{cc'} + 4S_d^{aa'} \gamma_\nu C \hat{S}_u^{Tbb'} C \gamma_\mu S_u^{cc'} + 4S_u^{aa'} \gamma_\nu C \hat{S}_d^{Tbb'} C \gamma_\mu S_u^{cc'} \\ & + 4S_u^{aa'} \gamma_\nu C S_d^{Tbb'} C \gamma_\mu \hat{S}_u^{cc'} + 4S_d^{aa'} \gamma_\nu C S_u^{Tbb'} C \gamma_\mu \hat{S}_u^{cc'} + 4S_u^{aa'} \gamma_\nu C S_u^{Tbb'} C \gamma_\mu \hat{S}_d^{cc'} \\ & + 2\hat{S}_u^{aa'} \operatorname{tr}[\gamma_\nu C S_u^{Tbb'} C \gamma_\mu S_d^{cc'}] + 2\hat{S}_u^{aa'} \operatorname{tr}[\gamma_\nu C S_d^{Tbb'} C \gamma_\mu S_u^{cc'}] + 2\hat{S}_d^{aa'} \operatorname{tr}[\gamma_\nu C S_u^{Tbb'} C \gamma_\mu S_u^{cc'}] \\ & + 2S_u^{aa'} \operatorname{tr}[\gamma_\nu C \hat{S}_u^{Tbb'} C \gamma_\mu S_d^{cc'}] + 2S_d^{aa'} \operatorname{tr}[\gamma_\nu C \hat{S}_u^{Tbb'} C \gamma_\mu S_u^{cc'}] + 2S_u^{aa'} \operatorname{tr}[\gamma_\nu C \hat{S}_d^{Tbb'} C \gamma_\mu S_u^{cc'}] \\ & + 2S_u^{aa'} \operatorname{tr}[\gamma_\nu C S_d^{Tbb'} C \gamma_\mu \hat{S}_u^{cc'}] + 2S_d^{aa'} \operatorname{tr}[\gamma_\nu C S_u^{Tbb'} C \gamma_\mu \hat{S}_u^{cc'}] + 2S_u^{aa'} \operatorname{tr}[\gamma_\nu C S_u^{Tbb'} C \gamma_\mu \hat{S}_d^{cc'}] \} \\ & + \sum_{q=u,d,s} e_q \sum_i \operatorname{tr}[S_q^{ii}(x_1, x_1) \gamma_\mu] \frac{1}{3} \epsilon^{abc} \epsilon^{a'b'c'} \{ 4S_u^{aa'} \gamma_\nu C S_u^{Tbb'} C \gamma_\mu S_d^{cc'} + 4S_u^{aa'} \gamma_\nu C S_d^{Tbb'} C \gamma_\mu S_u^{cc'} \\ & + 4S_d^{aa'} \gamma_\nu C S_u^{Tbb'} C \gamma_\mu \upsilon S_u^{cc'} + 2S_u^{aa'} \operatorname{tr}[\gamma_\nu C S_u^{Tbb'} C \gamma_\mu S_d^{cc'}] + 2S_u^{aa'} \operatorname{tr}[\gamma_\nu C S_d^{Tbb'} C \gamma_\mu S_u^{cc'}] \\ & + 2S_d^{aa'} \operatorname{tr}[\gamma_\nu C S_u^{Tbb'} C \gamma_\mu S_u^{cc'}] \}, \end{aligned} \tag{2.7}$$

where

$$\hat{S}_q^{aa'}(x_2, x_1, 0) = e_q \sum_i S_q^{ai}(x_2, x_1) \gamma_\alpha S_q^{ia'}(x_1, 0) \tag{2.8}$$

denotes the connected insertion of the probing current to a quark of charge e_q. Here we have explicitly selected the electromagnetic current. However, the present discussion may be generalized to any quark-field-based current operator bilinear in the quark fields.

The latter term of Eq. (2.7) accounts for the disconnected quark loop contribution depicted in Fig. 1(b). The sum over the quarks running around the loop has been restricted to the flavors relevant to the ground state baryon octet and decuplet. In the $SU(3)_{\text{flavor}}$ limit the sum vanishes for the electromagnetic current. However, the heavier strange quark mass allows for a nontrivial result. Because of the technical difficulties of numerically estimating M^{-1} for the squared lattice volume of diagonal spatial indices, these contributions have been omitted from lattice QCD calculations of electromagnetic structure in the spirit of QχPT, and we will also do so here. For other observables such as the scalar density or forward matrix elements of the axial vector current relevant to the spin of the baryon, the "charges" running around the loop do not sum to zero. In this case the second term of Eq. (2.7) can be just as significant as the connected term [19,20].

An examination of Eq. (2.7) reveals complete symmetry among the quark flavors in the correlation function. For example, wherever a d quark appears in the correlator, a u quark also appears in the same position in another term. An interesting consequence of this is that the connected insertion of the electromagnetic current for Δ^0 vanishes. All electromagnetic properties of the Δ^0 have their origin strictly in the disconnected loop contribution. Physically, what this means is that the valence wave functions for each of the quarks in the Δ resonances are identical under charge symmetry.

C. Two-point Green functions

In this and the following subsection discussing correlation functions at the hadronic level, the Dirac representation of the γ matrices is used to facilitate calculations of the γ-matrix algebra. It is then a simple task to account for the differences in γ-matrix and metric definitions in reporting the final results using Sakurai's notation.

The extraction of baryon mass and electromagnetic form factors proceeds through the calculation of the ensemble average (denoted $\langle \ldots \rangle$) of two- and three-point Green functions. The two-point function for decuplet baryons is defined as

$$\langle G_{\sigma\tau}^{BB}(t; \vec{p}; \Gamma) \rangle = \sum_{\vec{x}} e^{-i\vec{p}\cdot\vec{x}} \Gamma^{\beta\alpha} \langle \Omega | T(\chi_\sigma^\alpha(x) \bar{\chi}_\tau^\beta(0)) | \Omega \rangle. \tag{2.9}$$

Here Ω represents the QCD vacuum, Γ is a 4×4 matrix in Dirac space and α and β are Dirac indices. The subscripts σ and τ are the Lorentz indices of the spin-3/2 interpolating fields. At the hadronic level one proceeds by inserting a complete set of states $|B, p, s\rangle$ and defining

$$\langle \Omega | \chi_\sigma(0) | B, p, s \rangle = Z_B(p) \sqrt{\frac{M}{E_p}} u_\sigma(p, s), \tag{2.10}$$

where Z_B represents the coupling strength of $\chi_\sigma(0)$ to the baryon B. Our use of smeared interpolators makes this momentum dependent. Momentum is denoted by p, spin by s, and $u_\alpha(p, s)$ is a spin vector in the Rarita-Schwinger formalism. $E_p = \sqrt{\vec{p}^2 + M^2}$ and Dirac indices have been suppressed. Using the Rarita-Schwinger spin sum,

$$\begin{aligned} & \sum_s u_\sigma(p, s) \bar{u}_\tau(p, s) \\ & = -\frac{\gamma \cdot p + M}{2M} \left\{ g_{\sigma\tau} - \frac{1}{3} \gamma_\sigma \gamma_\tau - \frac{2 p_\sigma p_\tau}{3M^2} + \frac{p_\sigma \gamma_\tau - p_\tau \gamma_\sigma}{3M} \right\} \\ & \equiv \Lambda_{\sigma\tau}, \end{aligned} \tag{2.11}$$

our usual definitions for Γ,

$$\Gamma_j = \frac{1}{2}\begin{pmatrix} \sigma_j & 0 \\ 0 & 0 \end{pmatrix}; \qquad \Gamma_4 = \frac{1}{2}\begin{pmatrix} I & 0 \\ 0 & 0 \end{pmatrix}, \tag{2.12}$$

and $\vec{p} = (p, 0, 0)$, the large Euclidean time limit of the two-point function takes the form

$$\langle G^{BB}_{\sigma\tau}(t; \vec{p}, \Gamma_4)\rangle = Z_B(p)\bar{Z}_B(p)\frac{M}{E_p}e^{-E_p t}\,\mathrm{tr}[\Gamma_4 \Lambda_{\sigma\tau}], \tag{2.13}$$

where

$$\langle G^{BB}_{00}(t; \vec{p}, \Gamma_4)\rangle = Z_B(p)\bar{Z}_B(p)\frac{2}{3}\frac{|\vec{p}|^2}{M_B^2}\left(\frac{E_p + M_B}{2E_p}\right)e^{-E_p t}, \tag{2.14}$$

$$\langle G^{BB}_{11}(t; \vec{p}, \Gamma_4)\rangle = Z_B(p)\bar{Z}_B(p)\frac{2}{3}\frac{E_p^2}{M_B^2}\left(\frac{E_p + M_B}{2E_p}\right)e^{-E_p t}, \tag{2.15}$$

$$\langle G^{BB}_{22}(t; \vec{p}, \Gamma_4)\rangle = Z_B(p)\bar{Z}_B(p)\frac{2}{3}\left(\frac{E_p + M_B}{2E_p}\right)e^{-E_p t}, \tag{2.16}$$

$$\langle G^{BB}_{33}(t; \vec{p}, \Gamma_4)\rangle = Z_B(p)\bar{Z}_B(p)\frac{2}{3}\left(\frac{E_p + M_B}{2E_p}\right)e^{-E_p t}. \tag{2.17}$$

Here $\bar{Z}_B(p)$ denotes the overlap associated with our smeared source. $Z_B(p)$ is associated with the sink which need not have the same smearing.

Equations (2.14), (2.15), (2.16), and (2.17) provide four correlation functions from which a baryon mass may be extracted. All baryon masses extracted from the different selections of Lorentz indices agree within statistical uncertainties. The combination providing the smallest statistical fluctuations is $\langle G^{BB}_{22}(t; \vec{p}, \Gamma_4) + G^{BB}_{33}(t; \vec{p}, \Gamma_4)\rangle$ and these results are presented in Sec. V.

It should be noted that the spin-$3/2$ interpolating field also has overlap with spin-$1/2$ baryons. For the Δ baryons and Ω^- this poses no problem as these baryons are the lowest lying baryons in the mass spectrum having the appropriate isospin and strangeness quantum numbers. However, Σ^* and Ξ^* correlation functions may have lower lying octet spin-$1/2$ components allowed by flavor-symmetry breaking, $m_u = m_d \neq m_s$. Therefore it is desirable to use the spin-$3/2$ projection operator [21]

$$P^{3/2}_{\mu\nu}(p) = g_{\mu\nu} - \frac{1}{3}\gamma_\mu\gamma_\nu - \frac{1}{3p^2}(\gamma\cdot p\gamma_\mu p_\nu + p_\mu\gamma_\nu\gamma\cdot p). \tag{2.18}$$

However, our precision results for baryon two-point functions give no indication of a low-lying spin-$1/2$ component being excited by the spin-$3/2$ interpolating fields, and conclude such excitations are negligible.

D. Three-point functions and multipole form factors

Here we begin with a brief overview of the results of Ref. [22], where the multipole form factors are defined in terms of the covariant vertex functions and in terms of the current matrix elements. The electromagnetic current matrix element for spin-$3/2$ particles may be written as

$$\langle p', s'|j^\mu(0)|p, s\rangle = \sqrt{\frac{M_B^2}{E_p E_{p'}}}\bar{u}_\alpha(p', s')\mathcal{O}^{\alpha\mu\beta}u_\beta(p, s). \tag{2.19}$$

Here p and p' (s and s') denote the momentum (spin) of the initial and final states, respectively, and $u_\alpha(p, s)$ is a Rarita-Schwinger spin vector. The following Lorentz covariant form for the tensor

$$\mathcal{O}^{\alpha\mu\beta} = -g^{\alpha\beta}\left\{a_1\gamma^\mu + \frac{a_2}{2M_B}P^\mu\right\} - \frac{q^\alpha q^\beta}{(2M_B)^2}\left\{c_1\gamma^\mu + \frac{c_2}{2M_B}P^\mu\right\}, \tag{2.20}$$

where $P = p' + p$, $q = p' - p$ and M_B is the mass of the baryon, satisfies the standard requirements of invariance under time reversal, parity, G parity and gauge transformations. The parameters a_1, a_2, c_1 and c_2 are independent covariant vertex functions.

The multipole form factors are defined in terms of the covariant vertex functions through the following Lorentz invariant expressions [22]:

$$\mathcal{G}_{E0}(q^2) = (1 + \tfrac{2}{3}\tau)\{a_1 + (1 + \tau)a_2\} - \tfrac{1}{3}\tau(1 + \tau)\{c_1 + (1 + \tau)c_2\}, \tag{2.21}$$

$$\mathcal{G}_{E2}(q^2) = \{a_1 + (1 + \tau)a_2\} - \tfrac{1}{2}(1 + \tau)\{c_1 + (1 + \tau)c_2\}, \tag{2.22}$$

$$\mathcal{G}_{M1}(q^2) = (1 + \tfrac{4}{5}\tau)a_1 - \tfrac{2}{5}\tau(1 + \tau)c_1, \tag{2.23}$$

$$\mathcal{G}_{M3}(q^2) = a_1 - \tfrac{1}{2}(1 + \tau)c_1, \tag{2.24}$$

with $\tau = -q^2/(2M_B)^2 (\geq 0)$. The multipole form factors $\mathcal{G}_{E0}$, $\mathcal{G}_{E2}$, $\mathcal{G}_{M1}$ and $\mathcal{G}_{M3}$ are referred to as the charge ($E0$), electric-quadrupole ($E2$), magnetic-dipole ($M1$) and magnetic-octupole ($M3$) multipole form factors.

In a manner similar to that for the two-point function, the three-point Green function for the electromagnetic current is defined as

$$\begin{aligned}\langle G^{Bj^\mu B}_{\sigma\tau}(t_2,t_1;\vec p',\vec p;\Gamma)\rangle &= \sum_{\vec x_2,\vec x_1} e^{-i\vec p'\cdot\vec x_2} e^{+i(\vec p'-\vec p)\cdot\vec x_1}\\ &\quad\times \Gamma^{\beta\alpha}\langle\Omega|T(\chi^\alpha_\sigma(x_2)j^\mu(x_1)\bar\chi^\beta_\tau(0))|\Omega\rangle.\end{aligned}\tag{2.25}$$

Once again, the subscripts σ and τ are the Lorentz indices of the spin-$3/2$ interpolating fields. For large Euclidean time separations, $t_2 - t_1 \gg 1$ and $t_1 \gg 1$, the three-point function at the hadronic level becomes

$$\begin{aligned}\langle G^{Bj^\mu B}_{\sigma\tau}(t_2,t_1;\vec p',\vec p;\Gamma)\rangle &= \sum_{s,s'} e^{-E_{p'}(t_2-t_1)} e^{-E_p t_1}\Gamma^{\beta\alpha}\langle\Omega|\chi^\alpha_\sigma|p',s'\rangle\\ &\quad\times\langle p',s'|j^\mu|p,s\rangle\langle p,s|\bar\chi^\beta_\tau|\Omega\rangle,\end{aligned}\tag{2.26}$$

where the matrix element of the electromagnetic current is defined in (2.19), and the matrix elements of the interpolating fields are defined by Eq. (2.10).

The time dependence of the three-point function may be eliminated through the use of the two-point functions. Maintaining the lattice Ward identity, which guarantees the lattice electric form factor reproduces the total charge of the baryon at $q^2 = 0$, provides an indispensable guide to the optimum ratio of Green functions. The preferred ratio of two- and three-point Green functions is [7]

$$\begin{aligned}&R_\sigma{}^\mu{}_\tau(t_2,t_1;\vec p',\vec p;\Gamma)\\ &= \left(\frac{\langle G^{Bj^\mu B}_{\sigma\tau}(t_2,t_1;\vec p',\vec p;\Gamma)\rangle\langle G^{Bj^\mu B}_{\sigma\tau}(t_2,t_1;-\vec p,-\vec p';\Gamma)\rangle}{\langle G^{BB}_{\sigma\tau}(t_2;\vec p';\Gamma_4)\rangle\langle G^{BB}_{\sigma\tau}(t_2;-\vec p;\Gamma_4)\rangle}\right)^{1/2},\end{aligned}\tag{2.27}$$

$$\simeq \left(\frac{E_p + M}{2E_p}\right)^{1/2}\left(\frac{E_{p'} + M}{2E_{p'}}\right)^{1/2}\bar R_\sigma{}^\mu{}_\tau(\vec p',\vec p;\Gamma),\tag{2.28}$$

where we have defined the reduced ratio $\bar R_\sigma{}^\mu{}_\tau(\vec p',\vec p;\Gamma)$. Note that there is no implied sum over σ and τ in Eq. (2.27). Also, the square root in Eq. (2.27) spoils the covariant/contraviant nature of $R_\sigma{}^\mu{}_\tau$ and no meaning should be attached to the location of the indices. We still prefer this notation due to the close connection with $G^{Bj^\mu B}_{\sigma\tau}$.

Using our standard definitions for Γ given in Eq. (2.12) and the Rarita-Schwinger spin sum of Eq. (2.11), the multipole form factors may be isolated and extracted from the following combinations of $\bar R_\sigma{}^\mu{}_\tau(\vec p',\vec p;\Gamma)$:

$$\begin{aligned}\mathcal{G}_{E0}(q^2) &= \tfrac{1}{3}(\bar R_1{}^4{}_1(\vec q_1,0;\Gamma_4) + \bar R_2{}^4{}_2(\vec q_1,0;\Gamma_4)\\ &\quad + \bar R_3{}^4{}_3(\vec q_1,0;\Gamma_4)),\end{aligned}\tag{2.29}$$

$$\begin{aligned}\mathcal{G}_{E2}(q^2) &= 2\frac{M(E+M)}{|\vec q_1|^2}(\bar R_1{}^4{}_1(\vec q_1,0;\Gamma_4)\\ &\quad + \bar R_2{}^4{}_2(\vec q_1,0;\Gamma_4) - 2\bar R_3{}^4{}_3(\vec q_1,0;\Gamma_4)),\end{aligned}\tag{2.30}$$

$$\begin{aligned}\mathcal{G}_{M1}(q^2) &= -\frac{3}{5}\frac{E+M}{|\vec q_1|}(\bar R_1{}^3{}_1(\vec q_1,0;\Gamma_2) + \bar R_2{}^3{}_2(\vec q_1,0;\Gamma_2)\\ &\quad + \bar R_3{}^3{}_3(\vec q_1,0;\Gamma_2)),\end{aligned}\tag{2.31}$$

$$\begin{aligned}\mathcal{G}_{M3}(q^2) &= -4\frac{M(E+M)^2}{|\vec q_1|^3}\Big(\bar R_1{}^3{}_1(\vec q_1,0;\Gamma_2)\\ &\quad + \bar R_2{}^3{}_2(\vec q_1,0;\Gamma_2) - \frac{3}{2}\bar R_3{}^3{}_3(\vec q_1,0;\Gamma_2)\Big),\end{aligned}\tag{2.32}$$

where $\vec q_1 = (q,0,0)$. We note that smaller statistical uncertainties may be obtained for $\mathcal{G}_{E2}$ by using the symmetry

$$\bar R_2{}^4{}_2(\vec q_1,0;\Gamma_4) = \bar R_3{}^4{}_3(\vec q_1,0;\Gamma_4),\tag{2.33}$$

in Eq. (2.30). Hence, we define an average $\bar R^4_{\rm avg}$ as

$$\bar R^4{}_{\rm avg}(\vec q_1,0;\Gamma_4) = \tfrac{1}{2}[\bar R_2{}^4{}_2(\vec q_1,0;\Gamma_4) + \bar R_3{}^4{}_3(\vec q_1,0;\Gamma_4)].\tag{2.34}$$

With this definition the expression for $\mathcal{G}_{E2}(q^2)$ used in our simulations is

$$\begin{aligned}\mathcal{G}_{E2}(q^2) &= 2\frac{M(E+M)}{|\vec q_1|^2}(\bar R_1{}^4{}_1(\vec q_1,0;\Gamma_4)\\ &\quad - \bar R^4_{\rm avg}(\vec q_1,0;\Gamma_4)).\end{aligned}\tag{2.35}$$

III. LATTICE TECHNIQUES

The three-point functions discussed in Sec. II are constructed using the sequential source technique outlined in Refs. [7,23,24]. Our quenched gauge fields are generated with the $\mathcal{O}(a^2)$ mean-field improved Lüscher-Weisz plaquette plus rectangle gauge action [25] using the plaquette measure for the mean link. The simulations are performed on a $20^3 \times 40$ lattice with a lattice spacing of 0.128 fm as determined by the Sommer scale [26] $r_0 = 0.50$ fm. This provides a spatial length of 2.56 fm, allowing us to safely simulate at the lowest pion mass of 300 MeV. The large volume lattice also ensures a good density of low-lying momenta which are key to giving rise to chiral nonanalytic behavior in the observables simulated on the lattice [10,11]. Future studies should include additional volumes, in order to investigate any possible volume dependence of the three-point functions used to extract the form factors.

We perform a high-statistics analysis using a large sample of 400 configurations for our lightest eight quark masses. We also consider a subset of 200 configurations for the three heaviest quark masses in order to explore the approach to the heavy-quark regime. A small subensemble bias correction is applied multiplicatively to the heavy-quark results, by matching the central values of the 200 configuration subensemble and 400 configuration ensemble averages at $\kappa = 0.127\,80$. All tables display the raw, unbiased data for the first four kappa values. The first row of the $\kappa = 0.127\,80$ results gives the results from the

200 configuration subensembles, and the second gives the 400 configuration ensemble results. The scaled results from the 200 configuration subensembles are shown in the figures.

We use the fat-link irrelevant clover (FLIC) Dirac operator [27] which provides $\mathcal{O}(a)$ improvement [28]. The improved chiral properties of FLIC fermions allow efficient access to the light-quark-mass regime [29], making them ideal for dynamical fermion simulations now underway [30]. For the vector current, we use an $\mathcal{O}(a)$-improved FLIC conserved vector current [14]. We use a smeared source at $t_0 = 8$, and a current insertion centered at $t_1 = 14$. Complete details are described in Ref. [14].

Table I provides the kappa values used in our simulations, together with the calculated π and decuplet-baryon masses. While we refer to m_π^2 to infer the quark masses, we note that the critical value where the pion mass vanishes is $\kappa_{\rm cr} = 0.131\,35$.

We select $\kappa = 0.128\,85$ to represent the strange quark in this simulation. At this κ the $s\bar{s}$ pseudoscalar mass is 0.697 GeV, which compares well with the experimental value of $2m_{\rm K}^2 - m_\pi^2 = (0.693\ {\rm GeV})^2$, motivated by leading order chiral perturbation theory.

The error analysis of the correlation function ratios is performed via a third-order, single-elimination jackknife, with the χ^2 per degree of freedom ($\chi^2_{\rm dof}$) obtained via covariance matrix fits. We perform a series of fits through the ratios after the current insertion at $t_1 = 14$. By examining the $\chi^2_{\rm dof}$ we are able to establish a valid window through which we may fit in order to extract our observables. In all cases, we required a value of $\chi^2_{\rm dof}$ no larger than 1.5. The values of the static quantities quoted in this paper on a per quark-sector basis correspond to values for single quarks of unit charge.

When extracting form factors from the lattice correlation functions via the ratios defined in Eqs. (2.29), (2.30), (2.31), and (2.32) in Sec. II D, we employ the advanced analysis techniques outlined in detail in Ref. [14].

TABLE I. Hadron masses in units of GeV for various values of the hopping parameter κ. Pion masses are in GeV^2 while the baryon masses are in GeV.

κ	m_π^2	Δ	Σ^*	Ξ^*
0.126 30	0.9960(56)	1.999(9)	1.908(10)	1.815(11)
0.126 80	0.8936(56)	1.945(10)	1.871(11)	1.797(12)
0.127 30	0.7920(55)	1.890(10)	1.834(11)	1.779(13)
0.127 80	0.6920(54)	1.836(11)	1.798(12)	1.761(13)
0.127 80	0.6910(35)	1.845(10)	1.807(11)	1.770(11)
0.128 30	0.5925(33)	1.791(11)	1.771(11)	1.752(12)
0.128 85	0.4854(31)	1.732(12)	1.732(12)	1.732(12)
0.129 40	0.3795(31)	1.673(14)	1.693(13)	1.712(13)
0.129 90	0.2839(33)	1.622(16)	1.659(15)	1.695(13)
0.132 05	0.2153(35)	1.592(17)	1.638(15)	1.685(13)
0.130 60	0.1384(43)	1.565(18)	1.620(16)	1.676(14)
0.130 80	0.0939(44)	1.549(19)	1.609(16)	1.670(14)
Experiment	0.0196	1.232	1.382	1.531

The following calculations are performed in the lab frame $\vec{p} = 0$, $\vec{p}\,' = \vec{q} = |\vec{q}|\hat{x}$ at $|\vec{q}|a = 2\pi/L_x$ with $L_x = 20$, the minimum nonzero momentum available on our lattice. While q^2 is dependent on the mass of the baryon, we find this mass dependence to be small. Indeed all form factors may be regarded as being calculated at $Q^2 = -q^2 = 0.230 \pm 0.001\ {\rm GeV}^2$ where the error is dominated by the mass dependence of the target baryon. Where a spatial direction of the electromagnetic current is required, it is chosen to be the z direction.

IV. CORRELATION FUNCTION ANALYSIS

A. Baryon masses

Figure 2 is a plot of the decuplet-baryon masses along with the masses of the octet baryon from our previous calculation [14]. We observe the $SU(3)_{\rm flavor}$ limit at our sixth quark mass when $m_\pi^2 = 0.485(3)\ {\rm GeV}^2$. The mass of the Ω^- is the mass of the Δ at the $SU(3)_{\rm flavor}$ limit, i.e., 1.732 ± 0.012 GeV which differs from the experimentally measured value of 1.67 GeV by only about 3.6%. The higher value from the quenched simulation is in accord with the expectations of quenched χEFT [31,32]. The mass of the Δ baryon begins to show an upward chiral curvature as the m_π^2 becomes smaller. This behavior has already been discussed in Refs. [29,31,33].

In Fig. 3 we show the effective mass of the Δ as a function of time at the $SU(3)_{\rm flavor}$ limit. The fit result and error are denoted by the asterisk symbol on the left edge of

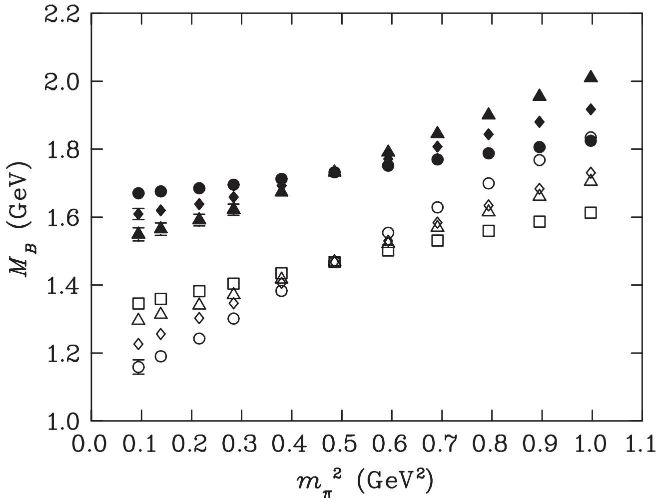

FIG. 2. Masses of the decuplet and the octet baryons [14] at different quark masses. At the lightest quark mass the lowest point is the nucleon (open circle), followed by Λ (open diamond), Σ (open triangle) and the Ξ (open square). The decuplet baryon with lowest mass is the Δ (closed triangle) followed by Σ^* (closed diamond) and Ξ^* (closed circle).

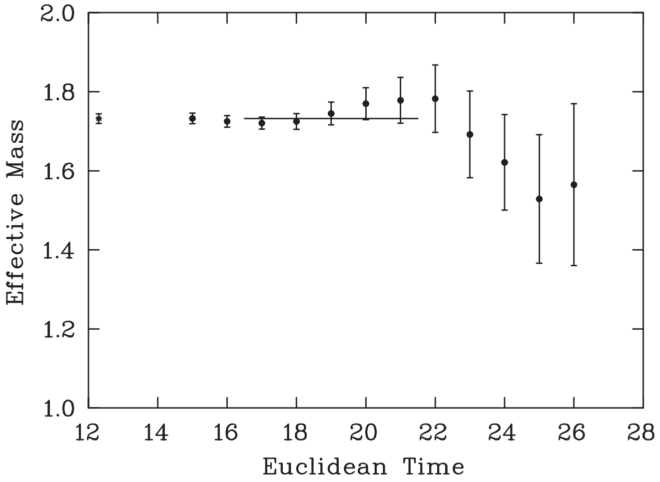

FIG. 3. Effective mass function of the Δ as a function of Euclidean time for $m_\pi^2 = 0.485(3)$ GeV^2, the $SU(3)_{\mathrm{flavor}}$ limit. The line indicates the fitting window and the best fit value. The asterisk at the left gives the fit result and the corresponding error.

the plot. Figure 4 shows the fit of the effective mass splitting for the Δ between the eighth and ninth quark masses. The final uncertainty combines this uncertainty with the error of the previous quark mass, the eighth in this case.

B. Form factor correlators

The baryon form factors are calculated on a quark-sector-by-quark-sector basis with each sector normalized to the contribution of a single quark with unit charge. Hence to calculate the corresponding baryon property, each quark-sector contribution should be multiplied by the appropriate charge and quark number. Under such a scheme for a generic form factor f, the Δ^+ form factor f_{Δ^+} is obtained from the u- and d-quark sectors normalized for a single quark of unit charge via

$$f_{\Delta^+} = 2 \times \tfrac{2}{3} \times f_u + 1 \times (-\tfrac{1}{3}) \times f_d. \qquad (4.1)$$

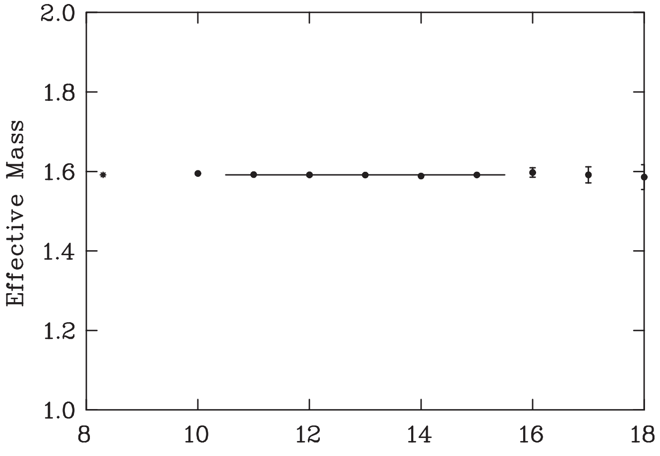

FIG. 4. Effective mass function of the Δ as a function of Euclidean time at the ninth quark mass where $m_\pi^2 = 0.215(4)$ GeV^2. The correlator is obtained from the splitting between the ninth and eighth quark-mass results. The line indicates the fitting window and the best fit value, and the asterisk gives the best fit with the corresponding error.

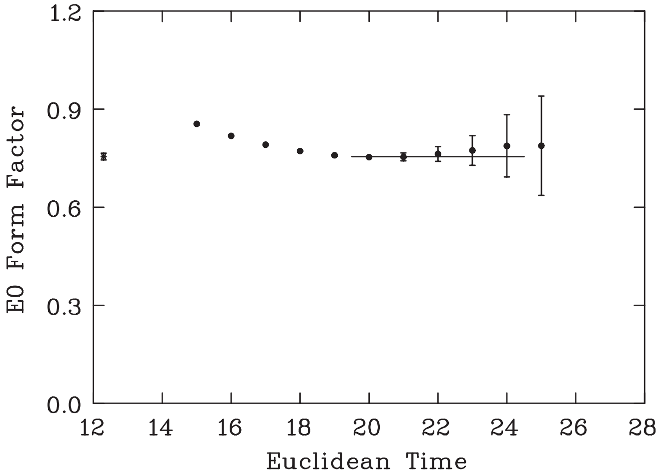

FIG. 5. $E0$ electric form factor of the u quark in the Δ at $Q^2 = 0.230(1)$ GeV^2 as a function of Euclidean time for $m_\pi^2 = 0.485(3)$ GeV^2, the $SU(3)_{\mathrm{flavor}}$ limit. The line indicates the fitting window and the best fit value with its error is shown by the asterisk on the left edge of the figure.

Figure 5 depicts the electric form factor $E0$ of the u quark in the Δ as a function of time at the $SU(3)_{\mathrm{flavor}}$ limit. The u and d quarks in the Δ states are identical as discussed in regard to Eq. (2.7). The straight lines indicate the

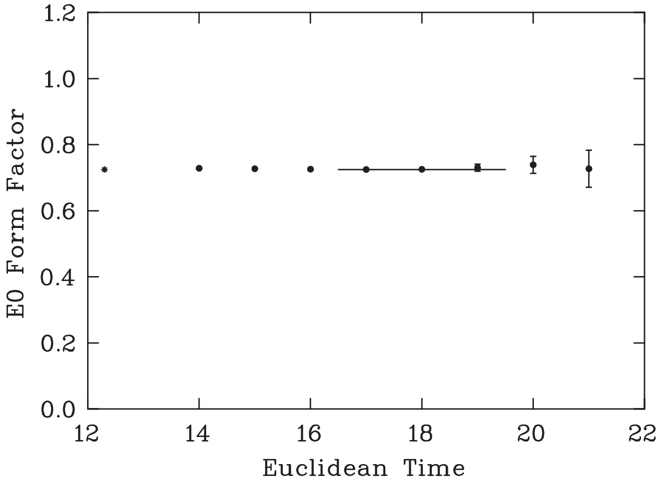

FIG. 6. $E0$ electric form factor of the u quark in the Δ at $Q^2 = 0.230(1)$ GeV^2 as a function of Euclidean time at the ninth quark mass where $m_\pi^2 = 0.215(4)$ GeV^2. The correlator is obtained from the splitting between the ninth and eighth quark-mass results. The line indicates the fitting window and the best fit value with its error is shown by the asterisk on the left edge of the figure.

TABLE II. Quark-sector contributions to the electric form factor $E0$ of the Δ at $Q^2 = 0.230(1)$ GeV^2. Sector contributions are for a single quark of unit charge. The fit windows are selected using the criteria outlined in Ref. [14]. The quark contribution at the $SU(3)$ limit when $m_\pi^2 = 0.485(3)$ GeV^2 provides the s quark contribution in Ω^-.

m_π^2		u_Δ			d_Δ	
(GeV^2)	Fit value	Fit window	$\chi^2_{\rm dof}$	Fit value	Fit window	$\chi^2_{\rm dof}$
0.9960(56)	0.800(5)	20–24	1.47	0.800(5)	20–24	1.47
0.8936(56)	0.794(6)	20–24	0.95	0.794(6)	20–24	0.95
0.7920(55)	0.788(7)	20–24	0.79	0.788(7)	20–24	0.79
0.6920(54)	0.783(8)	20–24	0.59	0.783(8)	20–24	0.59
0.6910(35)	0.773(6)	20–24	1.46	0.773(6)	20–24	1.46
0.5925(33)	0.764(7)	20–24	1.07	0.764(7)	20–24	1.07
0.4854(31)	0.755(10)	20–24	0.53	0.755(10)	20–24	0.53
0.3795(31)	0.744(11)	17–20	0.73	0.744(11)	17–20	0.73
0.2839(33)	0.733(13)	17–20	0.79	0.733(13)	17–20	0.79
0.2153(35)	0.725(16)	17–19	0.46	0.725(16)	17–19	0.46
0.1384(43)	0.717(22)	17–19	0.23	0.717(22)	17–19	0.23
0.0939(44)	0.693(33)	17–19	0.34	0.693(33)	17–19	0.34

TABLE III. Quark-sector contributions to the electric form factor $E0$ of Σ^* at $Q^2 = 0.230(1)$ GeV^2. Sector contributions are for a single quark having unit charge. The fit windows are selected using the criteria outlined in Ref. [14].

m_π^2		u_{Σ^*} or d_{Σ^*}			s_{Σ^*}	
(GeV^2)	Fit value	Fit window	$\chi^2_{\rm dof}$	Fit value	Fit window	$\chi^2_{\rm dof}$
0.9960(56)	0.804(6)	20–24	0.85	0.759(9)	20–24	0.54
0.8936(56)	0.798(7)	20–24	0.65	0.761(9)	20–24	0.50
0.7920(55)	0.792(8)	20–24	0.63	0.763(10)	20–24	0.49
0.6920(54)	0.786(9)	20–24	0.56	0.766(10)	20–24	0.48
0.6910(35)	0.774(6)	20–24	1.15	0.752(8)	20–24	0.97
0.5925(33)	0.764(8)	20–24	0.91	0.753(8)	20–24	0.79
0.4854(31)	0.755(10)	20–24	0.53	0.755(10)	20–24	0.53
0.3795(31)	0.744(11)	17–20	0.89	0.754(10)	17–20	0.22
0.2839(33)	0.733(12)	17–20	0.81	0.754(11)	17–20	0.37
0.2153(35)	0.727(14)	17–19	0.15	0.753(11)	17–19	0.21
0.1384(43)	0.719(18)	17–19	0.07	0.753(12)	17–19	0.05
0.0939(44)	0.710(23)	17–19	0.22	0.746(14)	17–19	0.63

TABLE IV. Quark-sector contributions to the electric form factor $E0$ of Ξ^* at $Q^2 = 0.230(1)$ GeV^2. Sector contributions are for a single quark having unit charge. The fit windows are selected using the criteria outlined in Ref. [14].

m_π^2		s_{Ξ^*}			u_{Ξ^*}	
(GeV^2)	Fit value	Fit window	$\chi^2_{\rm dof}$	Fit value	Fit window	$\chi^2_{\rm dof}$
0.9960(56)	0.765(10)	20–24	0.47	0.809(8)	20–24	0.66
0.8936(56)	0.766(11)	20–24	0.47	0.802(8)	20–24	0.58
0.7920(55)	0.767(11)	20–24	0.49	0.795(9)	20–24	0.61
0.6920(54)	0.769(12)	20–24	0.50	0.788(10)	20–24	0.58
0.6910(35)	0.753(9)	20–24	0.73	0.775(7)	20–24	0.89
0.5925(33)	0.754(9)	20–24	0.66	0.765(8)	20–24	0.75
0.4854(31)	0.755(10)	20–24	0.53	0.755(10)	20–24	0.53
0.3795(31)	0.754(10)	17–20	0.19	0.744(10)	17–20	1.19
0.2839(33)	0.754(10)	17–20	0.22	0.734(11)	17–20	0.77
0.2153(35)	0.754(10)	17–19	0.03	0.727(13)	17–19	0.09
0.1384(43)	0.755(11)	17–19	0.11	0.720(14)	17–19	0.10
0.0939(44)	0.754(11)	17–19	0.66	0.714(17)	17–19	0.19

TABLE V. The $E0$ form factors of the various charged decuplet baryons for different m_π^2 values. The $E0$ form factor of the Δ^- at the $SU(3)_{\rm flavor}$ limit [$m_\pi^2 = 0.485(3)$ GeV^2] provides the $E0$ form factor of the Ω^-.

m_π^2 (GeV^2)	Δ^{++}	Δ^+	Δ^-	Σ^{*+}	Σ^{*-}	Ξ^{*-}
0.9972(55)	1.601(10)	0.803(5)	−0.803(5)	0.819(6)	−0.789(7)	−0.780(9)
0.8936(56)	1.589(11)	0.794(6)	−0.794(6)	0.810(6)	−0.786(7)	−0.778(10)
0.7920(55)	1.577(13)	0.788(7)	−0.788(7)	0.801(7)	−0.782(8)	−0.777(10)
0.6920(54)	1.566(16)	0.783(8)	−0.783(8)	0.792(8)	−0.779(9)	−0.775(11)
0.6910(35)	1.545(11)	0.773(6)	−0.773(6)	0.781(6)	−0.766(7)	−0.760(8)
0.5925(33)	1.527(14)	0.764(7)	−0.764(7)	0.768(7)	−0.761(8)	−0.757(9)
0.4854(31)	1.509(19)	0.755(10)	−0.755(10)	0.755(10)	−0.755(10)	−0.755(10)
0.3795(31)	1.487(22)	0.744(11)	−0.744(11)	0.740(11)	−0.747(10)	−0.751(10)
0.2839(33)	1.465(26)	0.733(13)	−0.733(13)	0.726(13)	−0.741(12)	−0.747(11)
0.2153(35)	1.451(31)	0.725(16)	−0.725(16)	0.718(15)	−0.736(13)	−0.745(11)
0.1384(43)	1.433(44)	0.717(22)	−0.717(22)	0.708(20)	−0.730(15)	−0.743(12)
0.0939(44)	1.386(65)	0.693(33)	−0.693(33)	0.698(27)	−0.722(19)	−0.741(13)

fits which were selected using the $\chi^2_{\rm dof}$ considerations outlined in Ref. [14]. For light-quark masses smaller than the strange quark mass, we fit the change in the form factor correlation functions from one quark mass to the next and add this to the previous result at the heavier quark mass. This provides significant cancellation of correlated systematic errors and makes the selection of the fit regime transparent.

Figure 6 shows the fitting of the electric form factor splitting for the Δ^+ between the eighth and ninth quark masses, the latter having $m_\pi^2 = 0.215(4)$ GeV^2. The improvement of the plateau is apparent in Fig. 6. Still, substantial Euclidean time evolution is required to obtain an acceptable $\chi^2_{\rm dof}$.

Tables II, III, and IV list the electric form factors for all the decuplet baryons at the quark level for the 11 quark masses considered. In the tables, the selected time frame, the fit value and the associated $\chi^2_{\rm dof}$ are indicated. Table V provides collected results for the various decuplet baryons.

The magnetic form factor $M1$ for the u quark sector in the Δ at the $SU(3)$ limit is plotted in Fig. 7 as a function of Euclidean time. Here the conversion from the natural magneton $e/(2m_B)$, where the mass of the baryon under investigation appears, to the nuclear magneton $e/(2m_N)$, where the physical nucleon mass appears, has been done by multiplying the lattice form factor results by the ratio m_N/m_B. In this way the form factors are presented in terms of a constant unit, i.e., the nuclear magneton.

In Fig. 8 we present the Euclidean time dependence of the $M1$ magnetic form factors of the Δ, calculated at the ninth quark mass where $m_\pi^2 = 0.215(4)$ GeV^2 using the

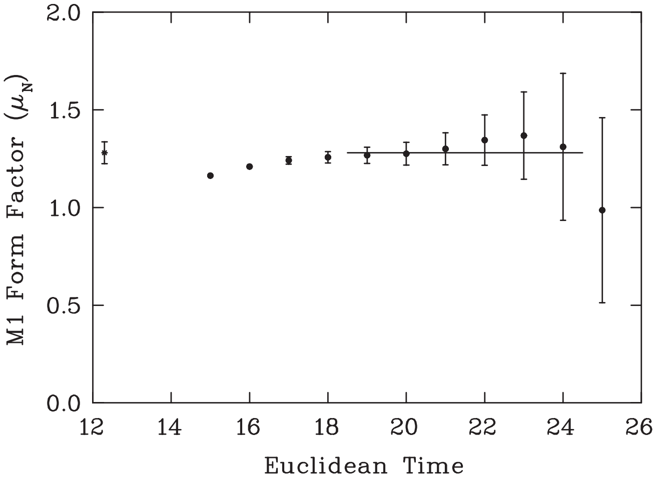

FIG. 7. $M1$ magnetic form factor of the u quark in Δ at $Q^2 = 0.230(1)$ GeV^2 as a function of Euclidean time for $m_\pi^2 = 0.485(3)$ GeV^2, the $SU(3)$-flavor limit. The line indicates the fitting window and the best fit value with its corresponding error is given by the asterisk on the left edge of the figure.

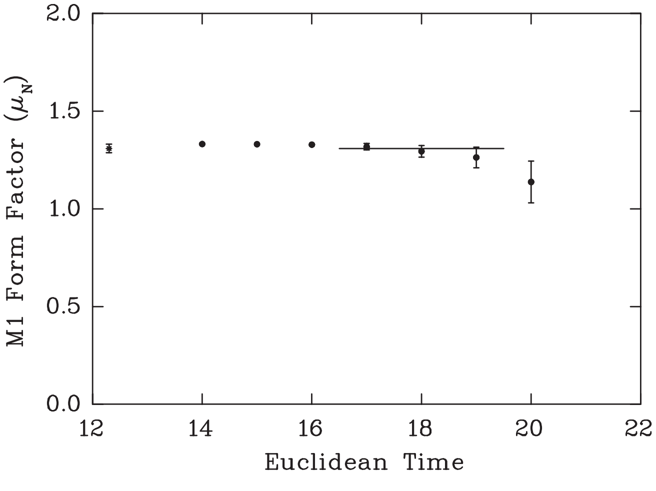

FIG. 8. $M1$ magnetic form factor of the u quark in Δ at $Q^2 = 0.230(1)$ GeV^2 at the ninth quark mass where $m_\pi^2 = 0.215(4)$ GeV^2. The correlator is obtained from the splitting between the ninth and eighth quark-mass results. The line indicates the fitting window and the best fit value with its error is shown by the asterisk on the left edge of the figure.

TABLE VI. Quark-sector contributions to the magnetic form factor $M1$ of the Δ at $Q^2 = 0.230(1)$ GeV^2. Sector contributions are for a single quark having unit charge. The fit windows are selected using the criteria outlined in Ref. [14]. The quark contribution at the $SU(3)_{\text{flavor}}$ limit when $m_\pi^2 = 0.4854(31)$ GeV^2 provides the s quark contribution in the Ω^-.

m_π^2 (GeV^2)		$u_\Delta(\mu_N)$			$d_\Delta(\mu_N)$	
	Fit value	Fit window	χ^2_{dof}	Fit value	Fit window	χ^2_{dof}
0.9960(56)	1.173(25)	19–24	1.45	1.173(25)	19–24	1.45
0.8936(56)	1.201(29)	19–24	1.14	1.201(29)	19–24	1.14
0.7920(55)	1.230(33)	19–24	0.95	1.230(33)	19–24	0.95
0.6920(54)	1.256(40)	19–24	0.75	1.256(40)	19–24	0.75
0.6910(35)	1.248(32)	19–24	1.25	1.248(32)	19–24	1.25
0.5925(33)	1.269(41)	19–24	0.79	1.269(41)	19–24	0.79
0.4854(31)	1.280(56)	19–24	0.31	1.280(56)	19–24	0.31
0.3795(31)	1.301(64)	17–21	1.37	1.301(64)	17–21	1.37
0.2839(33)	1.312(75)	17–19	1.14	1.312(75)	17–19	1.14
0.2153(35)	1.309(89)	17–19	0.91	1.309(89)	17–19	0.91
0.1384(43)	1.28(12)	17–18	1.26	1.28(12)	17–18	1.26
0.0939(44)	1.11(21)	17–18	1.79	1.11(21)	17–18	1.79

TABLE VII. Quark-sector contributions to the magnetic form factor $M1$ of the Σ^* at $Q^2 = 0.230(1)$ GeV^2. Sector contributions are for a single quark having unit charge. The fit windows are selected using the criteria outlined in Ref. [14].

m_π^2 (GeV^2)		u_{Σ^*} or $d_{\Sigma^*}(\mu_N)$			$s_{\Sigma^*}(\mu_N)$	
	Fit value	Fit window	χ^2_{dof}	Fit value	Fit window	χ^2_{dof}
0.9960(56)	1.191(31)	19–24	1.07	1.268(40)	19–24	0.51
0.8936(56)	1.216(35)	19–24	0.90	1.275(42)	19–24	0.49
0.7920(55)	1.242(39)	19–24	0.82	1.282(45)	19–24	0.47
0.6920(54)	1.264(45)	19–24	0.69	1.289(50)	19–24	0.47
0.6910(35)	1.254(37)	19–24	0.94	1.275(41)	19–24	0.69
0.5925(33)	1.272(45)	19–24	0.64	1.278(47)	19–24	0.51
0.4854(31)	1.280(56)	19–24	0.31	1.280(56)	19–24	0.31
0.3795(31)	1.297(62)	17–21	1.72	1.289(60)	17–21	0.70
0.2839(33)	1.306(68)	17–19	1.88	1.299(65)	17–19	0.04
0.2153(35)	1.305(76)	17–19	1.84	1.309(69)	17–19	0.08
0.1384(43)	1.299(89)	17–19	3.44	1.330(74)	17–19	0.44
0.0939(44)	1.25(12)	17–18	2.55	1.303(88)	17–18	0.16

TABLE VIII. Quark-sector contributions to the magnetic form factor $M1$ of the Ξ^* at $Q^2 = 0.230(1)$ GeV^2. Sector contributions are for a single quark having unit charge. The fit windows are selected using the criteria outlined in Ref. [14].

m_π^2 (GeV^2)		$s_{\Xi^*}(\mu_N)$			u_{Ξ^*} or $d_{\Xi^*}(\mu_N)$	
	Fit value	Fit window	χ^2_{dof}	Fit value	Fit window	χ^2_{dof}
0.9960(56)	1.286(50)	19–24	0.45	1.208(39)	19–24	0.84
0.8936(56)	1.289(52)	19–24	0.46	1.231(42)	19–24	0.79
0.7920(55)	1.293(54)	19–24	0.46	1.254(46)	19–24	0.76
0.6920(54)	1.297(56)	19–24	0.45	1.273(51)	19–24	0.63
0.6910(35)	1.278(48)	19–24	0.48	1.260(44)	19–24	0.68
0.5925(33)	1.280(51)	19–24	0.40	1.274(49)	19–24	0.52
0.4854(31)	1.280(56)	19–24	0.31	1.280(56)	19–24	0.31
0.3795(31)	1.285(58)	17–21	0.70	1.293(60)	17–21	2.56
0.2839(33)	1.289(60)	17–19	0.04	1.300(63)	17–19	2.66
0.2153(35)	1.293(62)	17–19	0.02	1.303(66)	17–19	1.44
0.1384(43)	1.302(64)	17–18	0.73	1.303(72)	17–18	2.36
0.0939(44)	1.301(67)	17–18	0.23	1.313(81)	17–18	0.56

TABLE IX. The magnetic $M1$ form factor of the charged decuplet baryons for different m_π^2 values. The $M1$ form factor of the Δ^- at the $SU(3)_{\text{flavor}}$ limit [$m_\pi^2 = 0.485(3)$ GeV^2] provides the $M1$ form factor of Ω^-.

m_π^2 (GeV^2)	Δ^{++}	Δ^+	Δ^-	Σ^{*+}	Σ^{*-}	Ξ^{*-}
0.9972(55)	2.35(5)	1.17(2)	−1.17(2)	1.16(3)	−1.22(3)	−1.26(5)
0.8936(56)	2.40(6)	1.20(3)	−1.20(3)	1.20(3)	−1.24(4)	−1.27(5)
0.7920(55)	2.46(7)	1.23(3)	−1.23(3)	1.23(4)	−1.26(4)	−1.28(5)
0.6920(54)	2.51(8)	1.26(4)	−1.26(4)	1.26(4)	−1.27(4)	−1.29(5)
0.6910(35)	2.50(6)	1.25(3)	−1.25(3)	1.25(4)	−1.26(4)	−1.27(5)
0.5925(33)	2.54(8)	1.27(4)	−1.27(4)	1.27(4)	−1.27(5)	−1.28(5)
0.4854(31)	2.56(11)	1.28(6)	−1.28(6)	1.28(6)	−1.28(6)	−1.28(6)
0.3795(31)	2.60(13)	1.30(6)	−1.30(6)	1.30(6)	−1.29(6)	−1.29(6)
0.2839(33)	2.62(15)	1.31(7)	−1.31(7)	1.31(7)	−1.30(7)	−1.29(6)
0.2153(35)	2.62(18)	1.31(9)	−1.31(9)	1.30(8)	−1.31(7)	−1.30(6)
0.1384(43)	2.56(24)	1.28(12)	−1.28(12)	1.29(10)	−1.31(8)	−1.30(6)
0.0939(44)	2.22(43)	1.11(22)	−1.11(22)	1.23(14)	−1.27(10)	−1.30(7)

splittings analysis. The onset of noise at this lighter quark mass is particularly apparent at time slice 20.

Results for the quark-sector contributions to the $M1$ magnetic form factors of the decuplet baryons are summarized in Tables VI, VII, and VIII. While some of the χ^2_{dof} are somewhat large we note that neighboring regimes with acceptable χ^2_{dof} have a variation in the central value that is small with respect to the statistical uncertainty. Results for the various decuplet baryons are given in Table IX.

V. DISCUSSION OF RESULTS

A. Charge radii

It is well known that the experimental electric (and magnetic) form factor of the proton is well described by a dipole ansatz at small Q^2

$$\mathcal{G}_E(Q^2) = \frac{\mathcal{G}_E(0)}{(1 + Q^2/m^2)^2}; \qquad Q^2 \geq 0. \tag{5.1}$$

This behavior has also been observed in recent lattice calculations [34]. Using this observation, together with the standard small Q^2 expansion of the Fourier transform of a spherical charge distribution,

$$\langle r_E^2 \rangle = -6 \frac{d}{dQ^2} \mathcal{G}_E(Q^2)|_{Q^2=0}, \tag{5.2}$$

we arrive at an expression which allows us to calculate the electric charge radius of a baryon using our two available values of the Sachs electric form factor [$\mathcal{G}_E(Q^2_{\text{min}})$, $\mathcal{G}_E(0)$], namely,

$$\frac{\langle r_E^2 \rangle}{\mathcal{G}_E(0)} = \frac{12}{Q^2}\left(\sqrt{\frac{\mathcal{G}_E(0)}{\mathcal{G}_E(Q^2)}} - 1\right). \tag{5.3}$$

However to calculate the charge radii of the neutral baryons, the above equation cannot be used, due to the fact that in those cases $\mathcal{G}_E = 0$. For the neutral baryons it becomes a simple matter to construct the charge radii by first calculating the charge radii for each quark sector. These quark sectors are then combined using the appropriate charge and quark number factors as described in Sec. IV B to obtain the total baryon charge radii. Indeed all baryon charge radii, including the charged states, are calculated in this manner.

Tables X, XI, and XII provide the electric charge radii of the decuplet baryons and the quark-sector contributions. Figures 9 and 10 depict plots of the quark contributions to the decuplet charge radii. At the $SU(3)$ limit (sixth quark mass) the quark contributions are identical in all cases as expected.

In Figs. 11 and 12 we compare the charge radii of the quark sectors in the decuplet baryons to those in the octet baryons at the ninth quark mass. From the figures it is

TABLE X. Charge radii of the Δ baryons for different m_π^2. Quark-sector contributions for a single quark of unit charge are included. The charge radii of the Δ^{++} are twice that of the Δ^+ and the results for the Δ^0 are 0 in quenched QCD. At the $SU(3)_{\text{flavor}}$ limit we find the charge radius of the Ω^- to be equal to $-0.307(15)$ fm^2.

m_π^2 (GeV^2)	u_Δ (fm^2)	d_Δ (fm^2)	Δ^+ (fm^2)	Δ^- (fm^2)
0.9960(56)	0.238(7)	0.238(7)	0.238(7)	−0.238(7)
0.8936(56)	0.247(8)	0.247(8)	0.247(8)	−0.247(8)
0.7920(55)	0.256(10)	0.256(10)	0.256(10)	−0.256(10)
0.6920(54)	0.264(12)	0.264(12)	0.264(12)	−0.264(12)
0.6910(35)	0.279(9)	0.279(9)	0.279(9)	−0.279(9)
0.5925(33)	0.293(11)	0.293(11)	0.293(11)	−0.293(11)
0.4854(31)	0.307(15)	0.307(15)	0.307(15)	−0.307(15)
0.3795(31)	0.324(17)	0.324(17)	0.324(17)	−0.324(17)
0.2839(33)	0.343(21)	0.343(21)	0.343(21)	−0.343(21)
0.2153(35)	0.355(26)	0.355(26)	0.355(26)	−0.355(26)
0.1384(43)	0.370(37)	0.370(37)	0.370(37)	−0.370(37)
0.0939(44)	0.410(57)	0.410(57)	0.410(57)	−0.410(57)

TABLE XI. Charge radii of the Σ^* baryons for different m_π^2. Quark-sector contributions for a single quark of unit charge are included.

m_π^2 (GeV^2)	u_{Σ^*} (fm^2)	s_{Σ^*} (fm^2)	Σ^{*+} (fm^2)	Σ^{*0} (fm^2)	Σ^{*-} (fm^2)
0.9960(56)	0.233(8)	0.299(13)	0.212(8)	−0.022(3)	−0.255(10)
0.8936(56)	0.242(10)	0.296(14)	0.224(9)	−0.018(2)	−0.260(11)
0.7920(55)	0.251(11)	0.293(15)	0.237(10)	−0.014(2)	−0.265(12)
0.6920(54)	0.260(13)	0.289(16)	0.250(12)	−0.010(2)	−0.270(14)
0.6910(35)	0.278(10)	0.311(12)	0.267(9)	−0.011(1)	−0.289(10)
0.5925(33)	0.292(12)	0.309(13)	0.286(11)	−0.006(1)	−0.298(12)
0.4854(31)	0.307(15)	0.307(15)	0.307(15)	0.000(1)	−0.307(15)
0.3795(31)	0.324(17)	0.308(16)	0.330(17)	0.006(1)	−0.319(16)
0.2839(33)	0.341(20)	0.309(17)	0.352(21)	0.011(1)	−0.330(19)
0.2153(35)	0.352(23)	0.309(17)	0.366(25)	0.014(2)	−0.338(21)
0.1384(43)	0.365(29)	0.311(18)	0.383(33)	0.018(5)	−0.347(25)
0.0939(44)	0.380(39)	0.321(22)	0.399(45)	0.020(7)	−0.360(32)

TABLE XII. Charge radii of the Ξ^* baryons for different m_π^2 values. Quark-sector contributions for a single quark of unit charge are included.

m_π^2 (GeV^2)	s_{Ξ^*} (fm^2)	u_{Ξ^*} (fm^2)	Ξ^{*0} (fm^2)	Ξ^{*-} (fm^2)
0.9960(56)	0.291(16)	0.227(11)	−0.042(5)	−0.269(14)
0.8936(56)	0.289(16)	0.236(12)	−0.035(5)	−0.271(14)
0.7920(55)	0.287(17)	0.246(13)	−0.027(4)	−0.273(15)
0.6920(54)	0.285(17)	0.256(14)	−0.019(3)	−0.275(16)
0.6910(35)	0.309(13)	0.276(11)	−0.022(3)	−0.298(12)
0.5925(33)	0.308(14)	0.291(13)	−0.011(2)	−0.302(14)
0.4854(31)	0.307(15)	0.307(15)	0.000(0)	−0.307(15)
0.3795(31)	0.307(15)	0.324(16)	0.011(1)	−0.313(16)
0.2839(33)	0.308(16)	0.341(19)	0.022(3)	−0.319(17)
0.2153(35)	0.307(16)	0.351(21)	0.029(4)	−0.322(17)
0.1384(43)	0.307(16)	0.363(24)	0.037(7)	−0.326(19)
0.0939(44)	0.308(17)	0.372(29)	0.043(10)	−0.330(20)

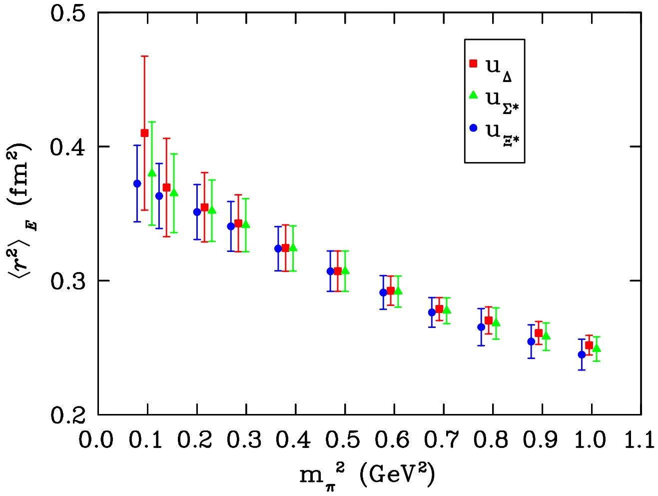

FIG. 9 (color online). Charge radii of the u quark in the Δ, Σ^* and Ξ^* at different quark masses. The values for the Δ are plotted at m_π^2 while that of the Σ^* and Ξ^* are plotted at shifted m_π^2 for clarity.

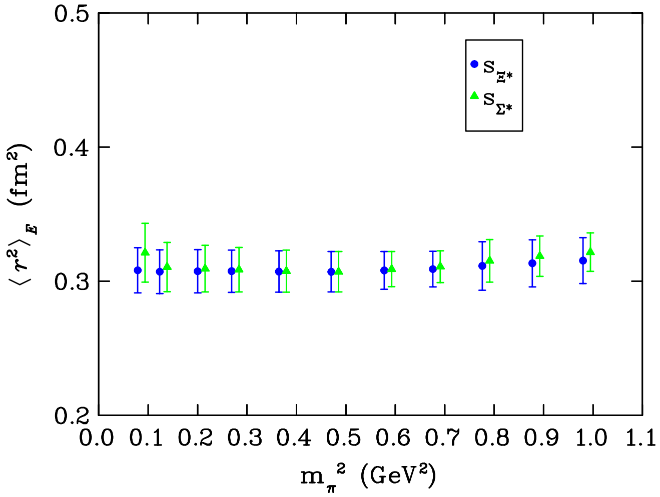

FIG. 10 (color online). Charge radii of the s quark in Σ^* and Ξ^* at different quark masses. The values for Σ^* are plotted at shifted m_π^2 values for clarity.

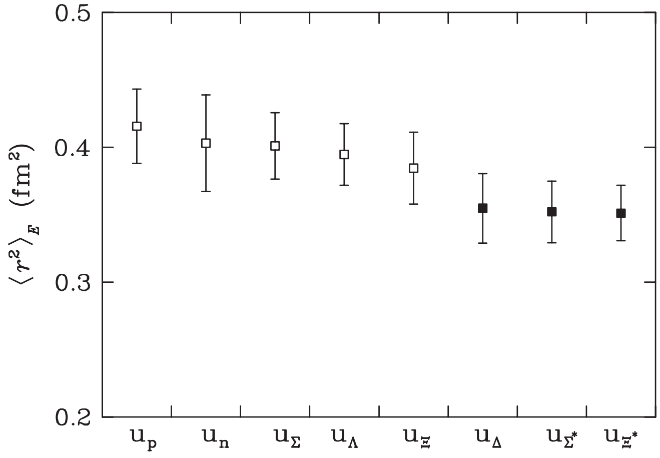

FIG. 11. Charge radii of the u quark sector in the octet (open squares) and the decuplet (filled squares) baryons at the ninth quark mass where $m_\pi^2 = 0.215(4)$ GeV^2.

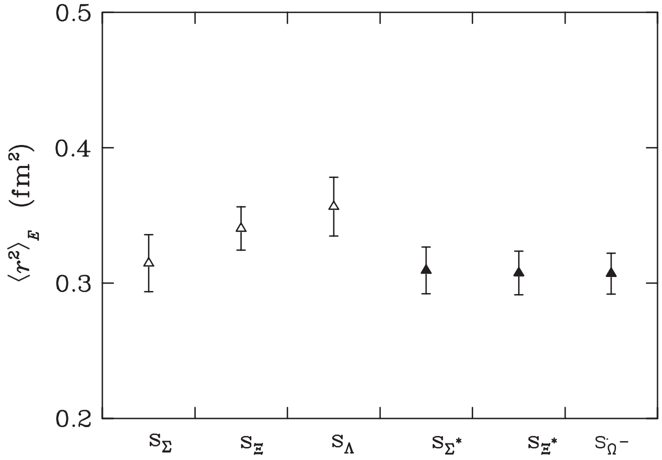

FIG. 12. Charge radii of the s quark sector in the octet (open squares) and the decuplet (filled squares) baryons at the ninth quark mass where $m_\pi^2 = 0.215(4)$ GeV^2.

evident that the contribution of the quarks is very much baryon dependent in the octet case, while for the decuplet baryons there is much less environmental sensitivity to the individual quark contributions. More specifically, in the case of the u quark in the octet baryons, the charge radius decreases with the inclusion of the s quark, while such an influence of the s quark on the u quark charge radius is absent in the decuplet baryons. Furthermore, we note that the charge radius of the u quark distribution in the decuplet baryons is *smaller* than that in the octet baryons.

From Fig. 11 it is evident that the charge radius of the u quark in the proton (u_p) is larger than that of the u quark in the Δ^+ (u_{Δ^+}). In order to investigate this difference more accurately, we compute the ratios of charge distributions of similar quarks in the octet to that in the decuplet. The uncertainty in the ratio $\langle r^2\rangle(u_p)/\langle r^2\rangle(u_{\Delta^+})$ is calculated using the jackknife method. Figures 13 and 14 depict the ratios of quark contributions in the octet baryons to those in the decuplet baryons at the $SU(3)_{\text{flavor}}$ limit and the ninth quark mass, respectively. In both cases, the doubly represented u quark contribution to the charge radius of octet baryons is larger than the singly represented octet quarks and decuplet quarks. At the $SU(3)$ limit, all quarks take the strange quark mass, and hence one would expect the quark model picture to dominate. This suggests that the u_Δ should have a broader distribution than that of the u_p due to hyperfine interactions. Our results contrast this prediction. The smaller charge radius of u_Δ compared to that of u_p also rules out any suggestion of a hyperfine attraction leading to ud diquark clustering in the nucleon or hyperon states [35].

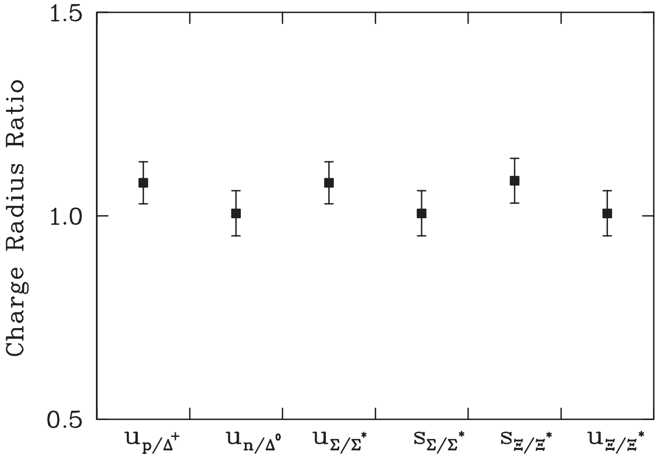

FIG. 13. Ratio of charge radii of the quark-sector contributions in the octet/decuplet baryons at the $SU(3)_{\text{flavor}}$ limit where $m_\pi^2 = 0.485(3)$ GeV^2.

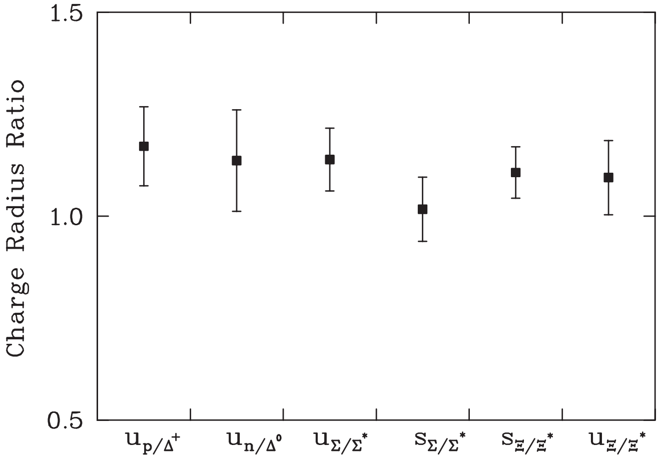

FIG. 14. Ratio of charge radii of the quark-sector contributions in the octet/decuplet baryons at the ninth quark mass where $m_\pi^2 = 0.215(4)$ GeV^2.

The charge radii of the various decuplet-baryon states are shown in Figs. 15–17 as a function of m_π^2. The charge

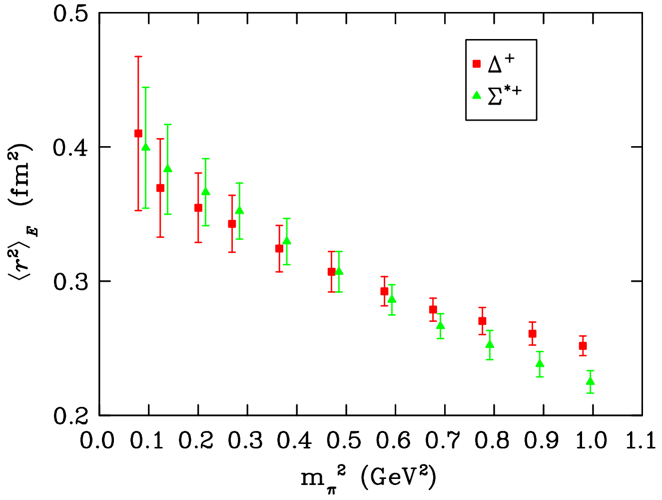

FIG. 15 (color online). Charge radii of the Δ^+ and Σ^{*+} at different quark masses. The values for Σ^* are plotted at shifted m_π^2 for clarity.

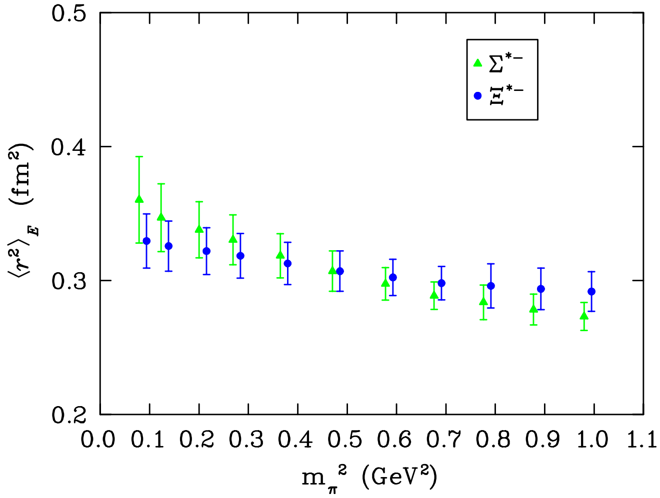

FIG. 16 (color online). Charge radii (magnitude) of the Σ^{*-} and Ξ^{*-} at different quark masses. The values for Ξ^{*-} are plotted at shifted m_π^2 for clarity.

radius of Δ^- is numerically equal to that of the Δ^+ with a negative sign. The charge radius of Ω^- is taken as that of the Δ^- in the $SU(3)_{\text{flavor}}$ limit, and is numerically equal to -0.307 ± 0.015 fm^2. As our calculations neglect the $\Omega^- \to \Xi^0\pi^-$ dressing, we anticipate our result to underestimate the magnitude.

The decuplet-baryon form factors are dominated by the net charge of the light quarks. For the Δ^0 the symmetry of the u and d quarks makes the form factors vanish. This is in contrast to the neutron where the three quarks are in mixed-symmetric states, giving rise to a nonzero form factor and charge radius. Charge radii of the neutral Σ^* and Ξ^* are also close to zero and are dominated by the light-quark sectors.

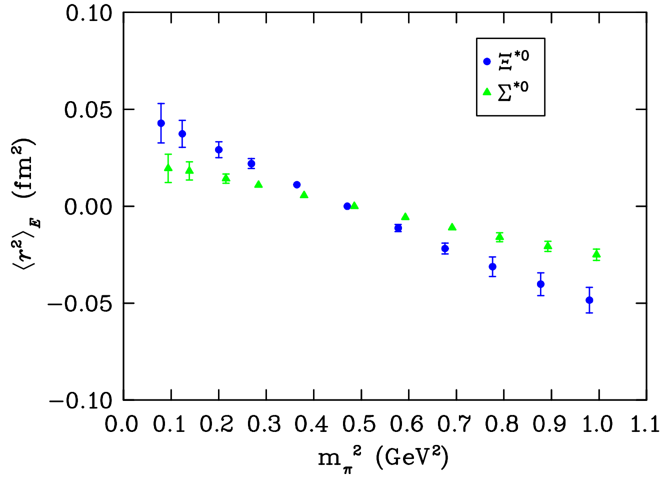

FIG. 17 (color online). Charge radii of the Σ^{*0} and Ξ^{*0} at different quark masses. The values for Σ^{*0} are plotted at shifted m_π^2 for clarity.

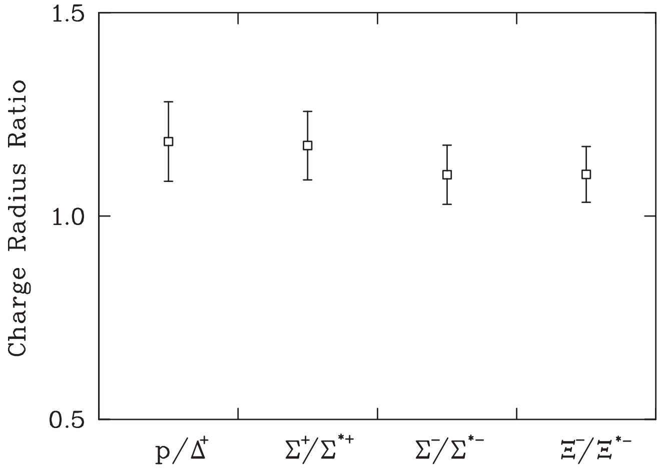

FIG. 18. Ratio of charge radii of the octet/decuplet baryons at the ninth quark mass where $m_\pi^2 = 0.215(4)$ GeV^2.

The presence of the s quark as one moves from the Δ to Σ^* and Ξ^* reduces the magnitude of the charge radius as indicated in Figs. 15–17. By examining the ratio of the charge radii of the octet to decuplet baryons in Fig. 18, we observe that the octet baryons have a slightly larger charge radius than their decuplet counterparts.

B. Magnetic moments

The magnetic moment is provided by the value of the magnetic form factor at zero momentum transfer $Q^2 = 0$,

$$\mu = \mathcal{G}_M(0)\frac{e}{2M_B}, \tag{5.4}$$

in units of the natural magneton, where M_B is the mass of the baryon. Since the magnetic form factors must be calculated at a finite value of momentum transfer Q^2, the magnetic moment must be inferred from our results, $\mathcal{G}_M(Q^2)$, obtained at the minimum nonvanishing momentum transfer available on our periodic lattice. We choose to scale our results from $\mathcal{G}_M(Q^2)$ to $\mathcal{G}_M(0)$. We do this by assuming that the Q^2 dependences of the electric and magnetic form factors are similar at the quark masses simulated herein. This is supported by experiment where the proton ratio $\frac{\mathcal{G}_M(Q^2)}{\mu\mathcal{G}_E(Q^2)} \simeq 1$ for values of Q^2 similar to that probed here. In this case

$$\mathcal{G}_M(0) = \frac{\mathcal{G}_M(Q^2)}{\mathcal{G}_E(Q^2)}\mathcal{G}_E(0). \tag{5.5}$$

The strange and light sectors of hyperons will scale differently, and therefore we apply Eq. (5.5) to the individual quark sectors for all the decuplet baryons. Decuplet-baryon properties are then reconstructed via

$$\mathcal{G}_M^B(0) = \mathcal{G}_M^l(0) + \mathcal{G}_M^s(0), \tag{5.6}$$

where l labels the light quarks and s labels the strange quark, and quark numbers and charges are included.

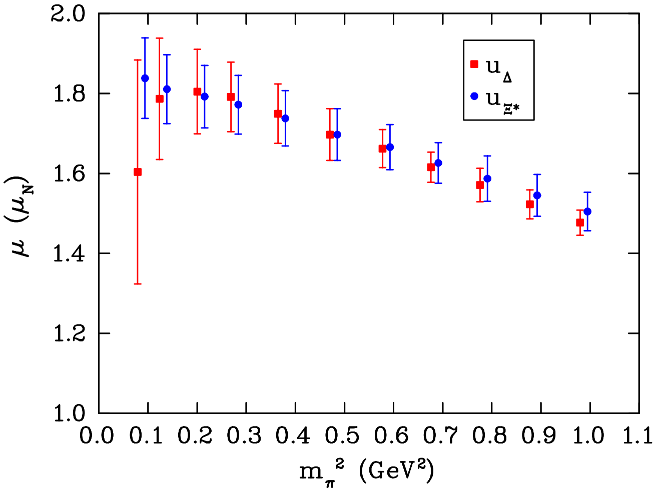

FIG. 19 (color online). Magnetic moments of a u quark in Δ and Ξ^* as a function of quark mass. The values for Ξ^* are plotted at shifted m_π^2 for clarity.

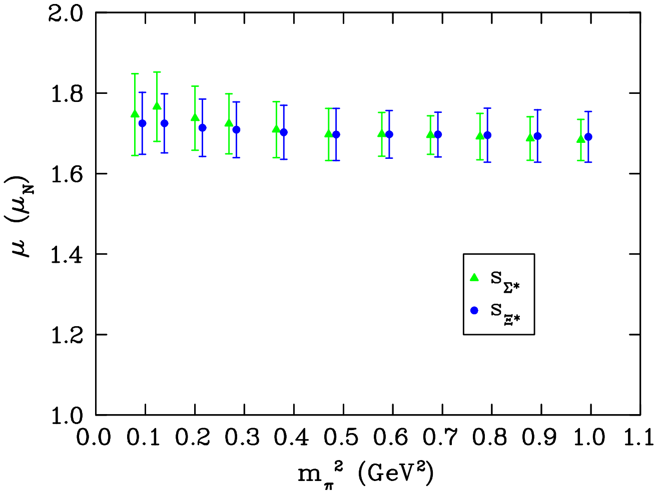

FIG. 21 (color online). The magnetic moments of the s quark sectors in the Σ^* and Ξ^* for different quark masses. The values for Ξ^* are plotted at shifted m_π^2 for clarity.

Similar calculations are performed for the u and d sectors of the Δ.

In Figs. 19–21, we display the quark-sector contributions to the decuplet magnetic moments, which are equal in the $SU(3)_{\text{flavor}}$ limit (sixth quark mass) for single quarks of unit charge. Here we observe that the quark contributions in the Σ^* and Ξ^* are very similar, which provides evidence that there is little environmental sensitivity. The behavior of the u_Δ as we approach the chiral regime is also very interesting.

C. Effective moments

In order to compare the decuplet moments with the octet moments from our previous lattice calculation [14], we construct so-called effective moments by equating the lattice quark-sector contributions to the same sector of the $SU(6)$-magnetic moment formula derived from $SU(6)$-spin-flavor-symmetry wave functions.

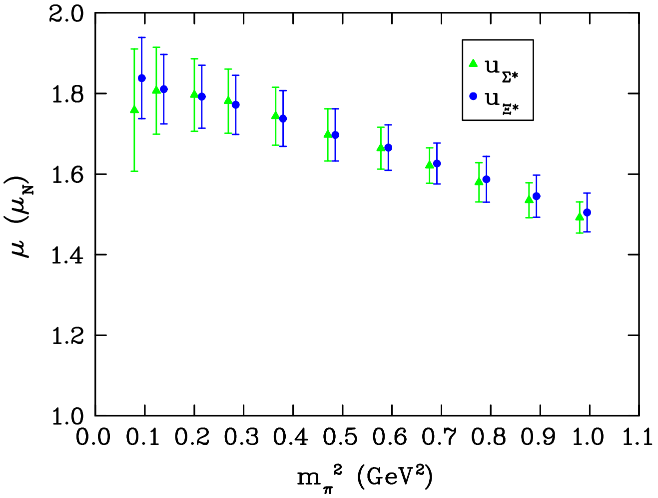

FIG. 20 (color online). Magnetic moments of a u quark in Σ^* and Ξ^* as a function of quark mass. The values for Ξ^* are plotted at shifted m_π^2 for clarity.

The simple quark model formula from $SU(6)$-spin-flavor symmetry gives the magnetic moment of the proton as

$$\mu_p = \tfrac{4}{3}\mu_u - \tfrac{1}{3}\mu_d, \tag{5.7}$$

where μ_u and μ_d are the intrinsic magnetic moments of the doubly represented u and singly represented d constituent quarks, respectively, per single quark. This can be generalized for any baryon with two doubly represented quarks D and one singly represented quark S. Focusing on the proton and using the charge factors of the doubly represented and singly represented quarks as $2/3$ and $(-1/3)$, respectively, we define effective moments for single quarks of unit charge μ^{Eff} by

$$\mu_u = \tfrac{2}{3}\mu_D^{\text{Eff}}, \qquad \mu_d = -\tfrac{1}{3}\mu_S^{\text{Eff}}, \tag{5.8}$$

such that Eq. (5.7) becomes

$$\mu_p = (\tfrac{4}{3})(\tfrac{2}{3})\mu_D^{\text{Eff}} - (\tfrac{1}{3})(-\tfrac{1}{3})\mu_S^{\text{Eff}}, \tag{5.9}$$

where the charge factors within μ_u and μ_d are now explicit.

On the lattice we calculate the baryon magnetic moments from the individual quark-sector contributions using

$$\mu_p = 2(\tfrac{2}{3})\mu_D^{\text{Latt}} + 1(-\tfrac{1}{3})\mu_S^{\text{Latt}}. \tag{5.10}$$

In the above equation the factors 2 and 1 in the first and second terms account for the number of doubly and singly represented quarks, respectively, while the charges are indicated in parentheses. Equating quark sectors in Eqs. (5.9) and (5.10) yields for the effective moments

$$\mu_S^{\text{Eff}} = -3\mu_S^{\text{Latt}}, \qquad \mu_D^{\text{Eff}} = \tfrac{3}{2}\mu_D^{\text{Latt}}. \tag{5.11}$$

One could also define a constituent-quark mass via

$$\mu_S^{\mathrm{Eff}} = \frac{e}{2m_S^{\mathrm{Eff}}}, \qquad \mu_D^{\mathrm{Eff}} = \frac{e}{2m_D^{\mathrm{Eff}}}, \tag{5.12}$$

revealing that $\mu_S^{\mathrm{Eff}} \simeq \mu_D^{\mathrm{Eff}}$ in most constituent-quark models.

For the decuplet baryons, the magnetic moment is the sum of the individual constituent-quark contributions. Hence Eq. (5.9) for the Δ baryons becomes

$$\mu_{\Delta^+} = 2(\tfrac{2}{3})\mu_D^{\mathrm{Eff}} + 1(-\tfrac{1}{3})\mu_S^{\mathrm{Eff}}. \tag{5.13}$$

On the lattice this is exactly the equation we use to build the decuplet-baryon moments from the quark-sector contributions. Therefore, the quark level magnetic moments that we calculate are the effective moments of the quarks for both the doubly and singly represented quarks, i.e.,

$$\mu^{\mathrm{Eff}} = \mu^{\mathrm{Latt}}. \tag{5.14}$$

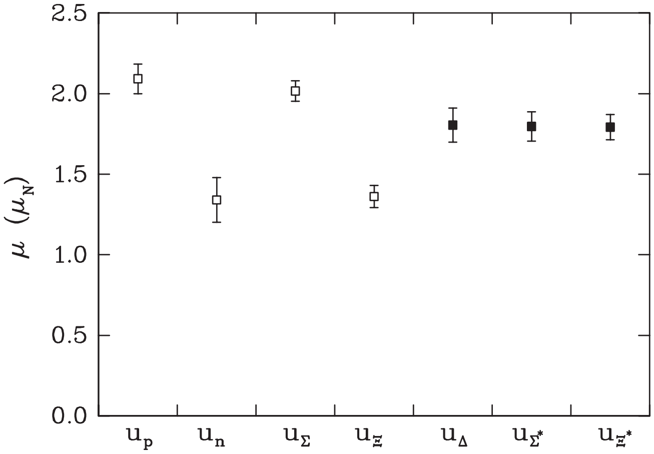

FIG. 22. Effective moments of the *u* quark sector in the octet and the decuplet baryons at the ninth quark mass where $m_\pi^2 = 0.215(4)$ GeV^2.

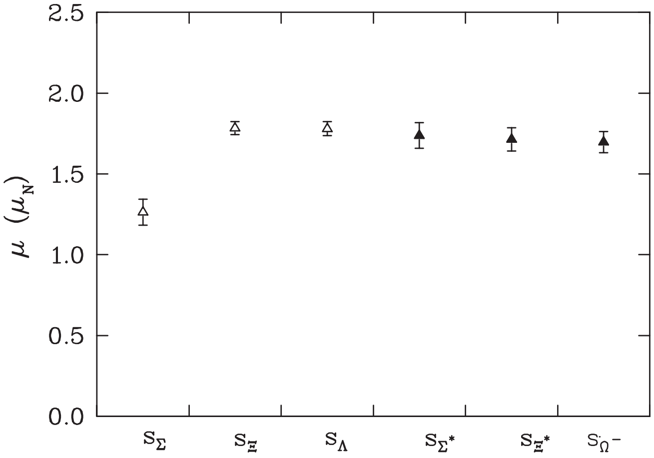

FIG. 23. Effective moments of the *s* quark sector in the octet and the decuplet baryons at the ninth quark mass where $m_\pi^2 = 0.215(4)$ GeV^2.

In Figs. 22 and 23 we plot the effective moments of the *u* and *s* quark sectors of the octet and decuplet baryons at the ninth quark mass. Here we observe that the quarks in the octet baryons show far more environmental sensitivity than their counterparts in the decuplet baryons.

The baryon magnetic moments are plotted in Figs. 24–26. For the magnetic moment of the Ω^- we take the value of μ_{Δ^-} at the $SU(3)$ limit viz., $-1.697 \pm 0.065\mu_N$, which is smaller than the value given by the Particle Data Group $(-2.02 \pm 0.05\mu_N)$.

This discrepancy could be partly due to the fact that the mass of Ω^- from our lattice calculation (1.73 ± 0.012 GeV) is slightly larger than the experimentally measured value (1.67 GeV).

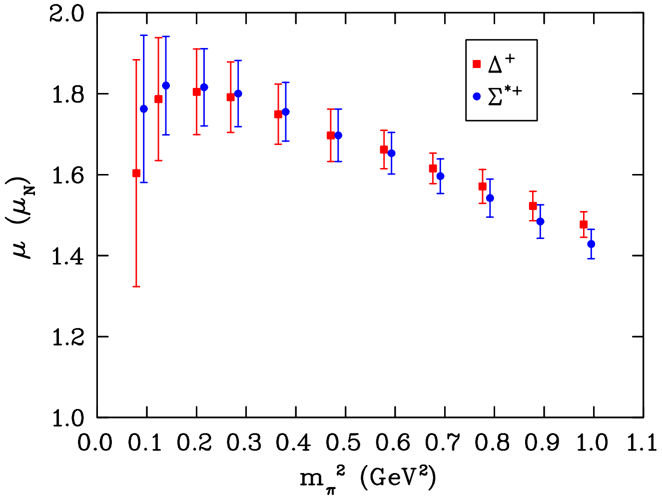

FIG. 24 (color online). Magnetic moments of Δ^+ and Σ^{*+} at different quark masses. The values for Σ^{*+} are plotted at shifted m_π^2 for clarity.

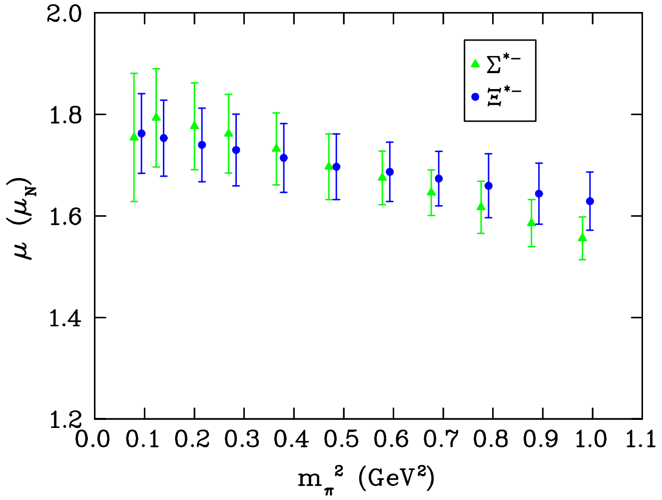

FIG. 25 (color online). Magnetic moments (magnitude) of Σ^{*-} and Ξ^{*-} at different quark masses. The values for Ξ^{*-} are plotted at shifted m_π^2 for clarity.

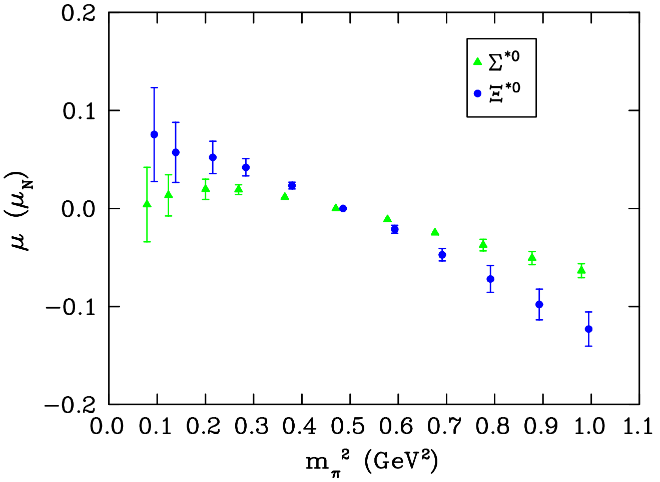

FIG. 26 (color online). Magnetic moments of Σ^{*0} and Ξ^{*0} at different quark masses. The values for Ξ^{*0} are plotted at shifted m_π^2 for clarity.

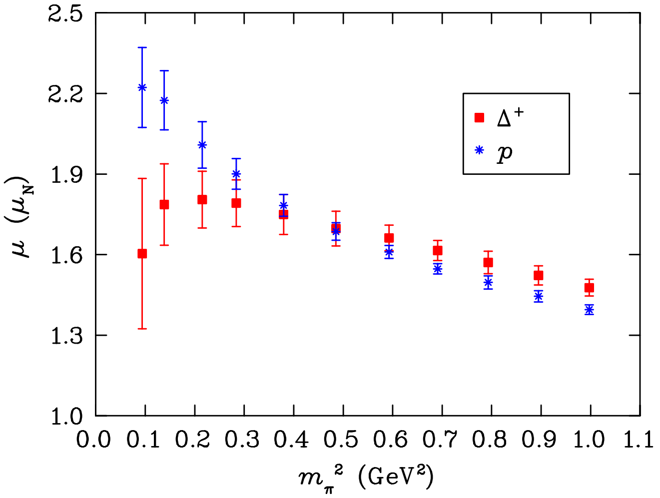

FIG. 27 (color online). Magnetic moments of Δ^+ and the proton at different quark masses.

Another reason for this discrepancy is likely to reside in the absence of $K\Xi$ loops in the virtual decay of Ω^-. The virtual transition $\Omega \to \Xi K$ requires the presence of a light sea-quark flavor, while in quenched QCD, there is only a heavy valence strange quark. In reality this would provide an important contribution, since Ξ is a lower mass state than Ω^-. The predominant contribution is $\Omega^0 \to \Xi^0 K^-$ with the z component of angular momentum in the positive direction. This process will act to enhance the magnitude of the negative moment. The absence of such loops in quenched QCD represents missing physics and causes the discrepancy from the values of full QCD. This is certainly a good place to search for dynamical sea-quark effects.

Figure 27 compares the magnetic moment of the Δ^+ with our earlier result for the proton magnetic moment on the same set of gauge field configurations [14]. A simple quark model predicts that the proton and the Δ^+ have equal magnetic moments. However the interplay between the different pion-loop contributions to the Δ^+ magnetic moments indicate that the proton magnetic moment should be greater than that of the Δ^+ in full QCD [36].

The presence of the $\Delta \to N\pi$ decay channel is particularly important for the quark-mass dependence of Δ properties [37]. Rapid curvature associated with this nonanalytic behavior is shifted to larger pion masses near the N-Δ mass splitting, $m_\pi \sim M_\Delta - M_N$. As described below, quenched-QCD decay-channel contributions come with a sign opposite to that of full QCD. This artifact holds tremendous promise for revealing unmistakable signatures of the quenched meson cloud.

The change in sign for the decay-channel contributions is easily understood through the consideration of the quark-flow diagrams in Fig. 28, illustrating the meson-cloud contributions to the Δ^{++} resonance in full QCD. Quark-flow diagram (a) corresponds to the hadronic process described in the top left diagram of Fig. 28. Since QCD is flavor-blind, the process illustrated in diagram (b) is equivalent to diagram (a) provided the masses of the u and d quarks are taken to be equal. On its own, diagram (b) describes the decay of the Δ^{++} to a doubly charged uuu

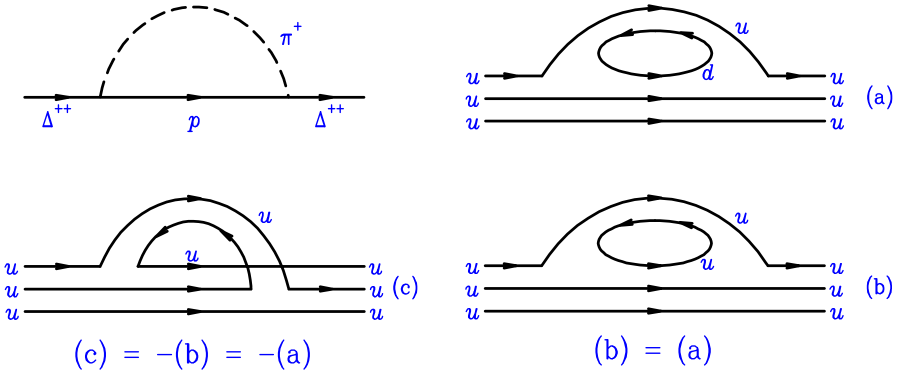

FIG. 28 (color online). Quark-flow diagrams for the meson-cloud contributions to the Δ^{++} in full QCD.

TABLE XIII. Magnetic moments of the Δ^+ in nuclear magnetons for different m_π^2. Quark-sector contributions for single quarks of unit charge are also provided. The magnetic moment of Δ^- is equal in magnitude to that of Δ^+ with a negative sign and the magnetic moment of the Δ^0 is 0. Charge symmetry also requires that the Δ^{++} has a magnetic moment twice that of Δ^+. The magnetic moment of Ω^- is that of Δ^- at the $SU(3)_{\mathrm{flavor}}$ limit where $m_\pi^2 = 0.4854(31)$ GeV^2, and takes the value $-1.697(65)\mu_N$.

m_π^2 GeV^2	$u_\Delta(\mu_N)$	$d_\Delta(\mu_N)$	$\Delta^+(\mu_N)$
0.9960(56)	1.466(31)	1.466(31)	1.466(31)
0.8936(56)	1.512(36)	1.512(36)	1.512(36)
0.7920(55)	1.559(42)	1.559(42)	1.559(42)
0.6920(54)	1.604(50)	1.604(50)	1.604(50)
0.6910(35)	1.615(38)	1.615(38)	1.615(38)
0.5925(33)	1.662(48)	1.662(48)	1.662(48)
0.4854(31)	1.697(65)	1.697(65)	1.697(65)
0.3795(31)	1.749(74)	1.749(74)	1.749(74)
0.2839(33)	1.792(87)	1.792(87)	1.792(87)
0.2153(35)	1.80(11)	1.80(11)	1.80(11)
0.1384(43)	1.79(15)	1.79(15)	1.79(15)
0.0939(44)	1.60(28)	1.60(28)	1.60(28)

TABLE XIV. Magnetic moments of Σ^*, Σ^{*0} and Σ^{*-} in nuclear magnetons with quark-sector contributions for a single quark of unit charge at different m_π^2 values.

m_π^2 GeV^2	$u_{\Sigma^*}(\mu_N)$	$s_{\Sigma^*}(\mu_N)$	$\Sigma^{*+}(\mu_N)$	$\Sigma^{*0}(\mu_N)$	$\Sigma^{*-}(\mu_N)$
0.9960(56)	1.482(38)	1.671(51)	1.418(36)	−0.063(7)	−1.545(42)
0.8936(56)	1.524(43)	1.675(54)	1.474(41)	−0.050(7)	−1.574(46)
0.7920(55)	1.568(48)	1.680(57)	1.531(47)	−0.037(6)	−1.605(51)
0.6920(54)	1.609(55)	1.683(62)	1.585(54)	−0.025(5)	−1.634(57)
0.6910(35)	1.621(44)	1.696(48)	1.596(43)	−0.025(3)	−1.646(45)
0.5925(33)	1.664(52)	1.698(54)	1.653(51)	−0.011(2)	−1.675(53)
0.4854(31)	1.697(65)	1.697(65)	1.697(65)	0.000(0)	−1.697(65)
0.3795(31)	1.744(72)	1.709(69)	1.755(72)	0.012(2)	−1.732(71)
0.2839(33)	1.781(80)	1.724(75)	1.800(82)	0.019(5)	−1.762(78)
0.2153(35)	1.796(90)	1.738(80)	1.816(95)	0.020(10)	−1.777(85)
0.1384(43)	1.81(11)	1.766(86)	1.82(12)	0.013(21)	−1.793(97)
0.0939(44)	1.76(15)	1.75(10)	1.76(18)	0.004(38)	−1.75(13)

TABLE XV. Magnetic moments of Ξ^{*0} and Ξ^{*-} in nuclear magnetons with quark-sector contributions for a single quark of unit charge at different m_π^2 values.

m_π^2 GeV^2	$s_{\Xi^*}(\mu_N)$	$u_{\Xi^*}(\mu_N)$	$\Xi^{*0}(\mu_N)$	$\Xi^{*-}(\mu_N)$
0.9960(56)	1.681(63)	1.494(48)	−0.124(18)	−1.619(57)
0.8936(56)	1.683(65)	1.534(52)	−0.099(16)	−1.633(60)
0.7920(55)	1.685(67)	1.576(56)	−0.073(14)	−1.649(63)
0.6920(54)	1.687(69)	1.615(62)	−0.048(11)	−1.663(67)
0.6910(35)	1.697(56)	1.626(51)	−0.047(6)	−1.674(54)
0.5925(33)	1.698(59)	1.666(57)	−0.021(4)	−1.687(58)
0.4854(31)	1.697(65)	1.697(65)	0.000(0)	−1.697(65)
0.3795(31)	1.703(67)	1.738(69)	0.023(4)	−1.714(68)
0.2839(33)	1.709(69)	1.772(73)	0.042(9)	−1.730(70)
0.2153(35)	1.714(71)	1.792(78)	0.052(16)	−1.740(73)
0.1384(43)	1.725(73)	1.811(86)	0.057(31)	−1.753(75)
0.0939(44)	1.725(77)	1.84(10)	0.076(48)	−1.763(79)

"proton," which we denote p^{++}. Of course, such states do not exist in full QCD and diagram (c) provides a contribution which is exactly equal but opposite in sign to diagram (b) when the intermediate state is a *uuu* proton. Upon quenching the theory, both diagrams (a) and (b) are eliminated, leaving only diagram (c). Hence the physics of the $\Delta \to N\pi$ decay is present in the quenched approximation [32] but its contribution has the wrong sign. This signature of quenched chiral physics is manifest in our results.

All the decuplet baryons show, to some extent, a turnover of the magnetic moment in the low quark-mass region just above the opening of the $N\pi$ decay channel. The magnitude of the turnover is dampened by the presence of a strange quark, which is seen by the fact that the Σ^* has a smaller turnover than the Δ. The Ξ baryons with two *s* quarks only admit kaon loops and do not display a turnover, further clarifying a link to chiral physics.

The magnetic moments of the decuplet baryons are listed in Tables XIII, XIV, and XV.

D. Electric-quadrupole form factors

The $E2$ form factors of the spin-$3/2$ decuplet baryons provide interesting information about the distribution of charge and its deviation from spherical symmetry. In Fig. 29 we show the correlation function proportional to the $E2$ quadrupole form factor of the *u* quark in the Δ at the $SU(3)_{\text{flavor}}$ limit, in units of e/M_N^2, as a function of Euclidean time. Figure 30 indicates the quadrupole form factor of the *u* quark in the Δ at the ninth quark mass. Here the employment of the splittings technique facilitates the extraction of the signal. In both cases a nontrivial result is obtained. As mentioned in Sec. II D, we consider the symmetry of the last two terms in Eq. (2.35) as the deciding factor in selecting the upper limit of the fit window.

The quark-sector contributions to the form factors in units of e/M_N^2 of all the decuplet members are indicated in Tables XVI, XVII, and XVIII. For an axially deformed object the quadrupole form factor is related to the charge distribution in the Breit frame through [7]

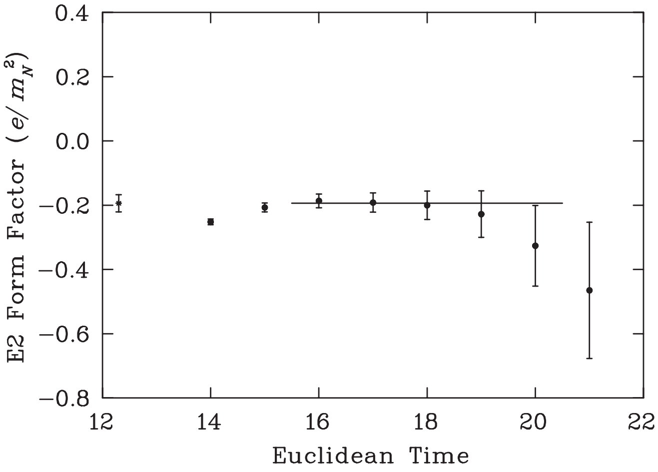

FIG. 29. $E2$ electric form factor of the *u* or *d* quark sector of the Δ at the $SU(3)_{\text{flavor}}$ limit as a function of Euclidean time.

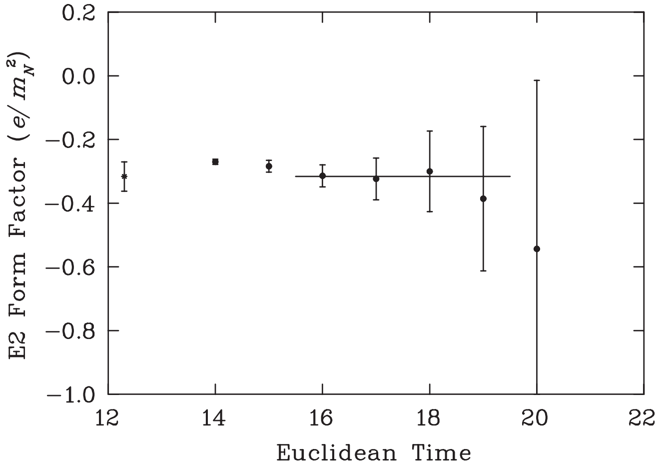

FIG. 30. $E2$ electric form factor of the *u* or *d* quark sector of the Δ as a function of Euclidean time at the ninth quark mass where $m_\pi^2 = 0.215(4)$ GeV^2.

$$\mathcal{G}_{E2}(0) = M_B^2 \int d^3 r \bar{\psi}(r)(3z^2 - r^2)\psi(r), \tag{5.16}$$

where $3z^2 - r^2$ is the standard operator used for quadrupole moments. A positive quadrupole form factor for a positively charged baryon indicates a prolate charge distribution, while a negative quadrupole form factor indicates an oblate charge distribution. In nonrelativistic models, the $E2$ form factor vanishes unless some configuration mixing of higher orbital-angular momentum states is included in the baryon ground state.

The $E2$ form factors of the charged decuplet baryons in units of fm^2 for different values of m_π^2 are listed in Table XIX. The $E2$ form factor of the Δ^0 is identically equal to zero and for the other neutral baryons, it is close to zero. The results for the charged decuplet baryons are nonzero, indicating that they have a deformed shape.

The quark-sector contributions to the $E2$ form factors are shown in Figs. 31–33. Once again, the importance of chiral physics is beginning to manifest itself in these results. A significant enhancement of the magnitude of the light-quark-sector contribution to the $E2$ form factor is observed in the Δ as the opening of the $N\pi$ decay channel is approached. A similar effect is seen, to a lesser extent, in the Σ^*, while for the Ξ^- no chiral curvature is observed due to the two *s* quarks admitting only kaon loops, as discussed in the previous section. The $E2$ form factors for the various decuplet baryons are shown in Figs. 34–36.

From our simulation we conclude that the $E2$ form factor of the Ω^- baryon [the value of the Δ^- form factor at $SU(3)_{\text{flavor}}$ limit] is $(0.86 \pm 0.12) \times 10^{-2}$ fm^2. The accuracy of our result indicates a definite nonzero value of

TABLE XVI. Quark-sector contributions to the $E2$ form factor of Δ at $Q^2 = 0.230(1)\ \mathrm{GeV}^2$ in fixed units of e/m_N^2. Sector contributions are for a single quark having unit charge. The fit windows are selected using the criteria outlined in Ref. [14].

m_π^2 (GeV^2)		u_Δ			d_Δ	
	Fit value	Fit window	χ^2_{dof}	Fit value	Fit window	χ^2_{dof}
0.9960(56)	−0.117(16)	16–20	1.63	−0.117(16)	16–20	1.63
0.8936(56)	−0.123(18)	16–20	1.39	−0.123(18)	16–20	1.39
0.7920(55)	−0.130(22)	16–20	1.16	−0.130(22)	16–20	1.16
0.6920(54)	−0.137(26)	16–20	1.01	−0.137(26)	16–20	1.01
0.6910(35)	−0.163(17)	16–20	0.76	−0.163(17)	16–20	0.76
0.5925(33)	−0.177(21)	16–20	0.75	−0.177(21)	16–20	0.75
0.4854(31)	−0.194(27)	16–20	0.86	−0.194(27)	16–20	0.86
0.3795(31)	−0.218(40)	16–19	1.03	−0.218(40)	16–19	1.03
0.2839(33)	−0.263(67)	16–19	1.57	−0.263(67)	16–19	1.57
0.2153(35)	−0.32(11)	16–19	1.20	−0.32(11)	16–19	1.20
0.1384(43)	−0.52(20)	16–18	0.72	−0.52(20)	16–18	0.72
0.0939(44)	−0.68(26)	15–16	1.06	−0.68(26)	15–16	1.06

TABLE XVII. Quark-sector contributions to the $E2$ form factor of Σ^* at $Q^2 = 0.230(1)\ \mathrm{GeV}^2$ in units of e/m_N^2. Sector contributions are for a single quark having unit charge. The fit windows are selected using the criteria outlined in Ref. [14].

m_π^2 (GeV^2)		u_{Σ^*} or d_{Σ^*}			s_{Σ^*}	
	Fit value	Fit window	χ^2_{dof}	Fit value	Fit window	χ^2_{dof}
0.9960(56)	−0.132(19)	16–20	1.52	−0.113(29)	16–20	0.75
0.8936(56)	−0.136(22)	16–20	1.36	−0.118(31)	16–20	0.71
0.7920(55)	−0.145(25)	16–20	1.20	−0.124(33)	16–20	0.66
0.6920(54)	−0.147(29)	16–20	1.07	−0.131(36)	16–20	0.65
0.6910(35)	−0.172(18)	16–20	0.91	−0.170(22)	16–20	0.48
0.5925(33)	−0.183(22)	16–20	0.89	−0.180(24)	16–20	0.61
0.4854(31)	−0.194(27)	16–20	0.86	−0.194(27)	16–20	0.86
0.3795(31)	−0.208(36)	16–20	0.48	−0.211(32)	16–20	1.89
0.2839(33)	−0.225(51)	16–17	0.41	−0.231(38)	16–17	0.61
0.2153(35)	−0.233(73)	16–19	1.08	−0.257(48)	16–19	1.84
0.1384(43)	−0.29(11)	16–17	1.71	−0.300(67)	16–17	1.07
0.0939(44)	−0.42(16)	16–17	0.94	−0.325(88)	16–17	0.31

TABLE XVIII. Quark-sector contributions to the $E2$ form factor of Ξ^* at $Q^2 = 0.230(1)\ \mathrm{GeV}^2$ in units of e/m_N^2. Sector contributions are for a single quark having unit charge. The fit windows are selected using the criteria outlined in Ref. [14].

m_π^2 (GeV^2)		s_{Ξ^*}			u_{Ξ^*} or d_{Ξ^*}	
	Fit value	Fit window	χ^2_{dof}	Fit value	Fit window	χ^2_{dof}
0.9960(56)	−0.127(36)	16–20	0.64	−0.157(25)	16–20	1.75
0.8936(56)	−0.131(37)	16–20	0.64	−0.157(27)	16–20	1.52
0.7920(55)	−0.136(39)	16–20	0.64	−0.159(30)	16–20	1.35
0.6920(54)	−0.141(40)	16–20	0.66	−0.159(33)	16–20	1.18
0.6910(35)	−0.180(24)	16–20	0.65	−0.184(20)	16–20	1.17
0.5925(33)	−0.186(25)	16–20	0.73	−0.190(23)	16–20	1.04
0.4854(31)	−0.194(27)	16–20	0.86	−0.194(27)	16–20	0.86
0.3795(31)	−0.201(29)	16–17	0.82	−0.198(33)	16–21	0.62
0.2839(33)	−0.208(31)	16–17	0.59	−0.200(41)	16–17	0.23
0.2153(35)	−0.214(34)	16–17	0.80	−0.191(52)	16–17	0.06
0.1384(43)	−0.222(38)	16–17	0.92	−0.184(71)	16–18	0.34
0.0939(44)	−0.222(41)	15–16	0.17	−0.183(82)	15–16	0.70

TABLE XIX. *E*2 form factors at $Q^2 = 0.230(1)$ GeV^2 of the charged decuplet baryons in units of 10^{-2} fm^2 for different m_π^2 values. The *E*2 form factor of the Δ^- at the $SU(3)_{\text{flavor}}$ limit where $m_\pi^2 = 0.485(3)$ provides the *E*2 form factor of the Ω^-.

m_π^2 (GeV^2)	Δ^{++}	Δ^+	Δ^-	Σ^{*+}	Σ^{*-}	Ξ^{*-}
0.9972(55)	−1.03(14)	−0.517(69)	0.517(69)	−0.613(77)	0.555(97)	0.60(14)
0.8936(56)	−1.08(16)	−0.541(80)	0.541(80)	−0.629(88)	0.57(11)	0.62(15)
0.7920(55)	−1.15(19)	−0.575(96)	0.575(96)	−0.65(10)	0.60(12)	0.63(16)
0.6920(54)	−1.21(23)	−0.61(12)	0.61(12)	−0.67(12)	0.63(14)	0.65(17)
0.6910(35)	−1.44(15)	−0.718(75)	0.718(75)	−0.765(77)	0.757(86)	0.80(10)
0.5925(33)	−1.56(18)	−0.782(91)	0.782(91)	−0.813(92)	0.804(99)	0.83(11)
0.4854(31)	−1.71(24)	−0.86(12)	0.86(12)	−0.86(12)	0.86(12)	0.86(12)
0.3795(31)	−1.93(35)	−0.96(18)	0.96(18)	−0.91(17)	0.92(15)	0.88(13)
0.2839(33)	−2.32(59)	−1.16(29)	1.16(29)	−0.99(25)	1.00(20)	0.91(15)
0.2153(35)	−2.79(95)	−1.40(48)	1.40(48)	−0.99(37)	1.07(28)	0.91(17)
0.1384(43)	−4.6(1.8)	−2.31(88)	2.31(88)	−1.28(58)	1.30(41)	0.92(21)
0.0939(44)	−6.0(2.3)	−3.0(1.1)	3.0(1.1)	−1.99(86)	1.71(57)	0.92(23)

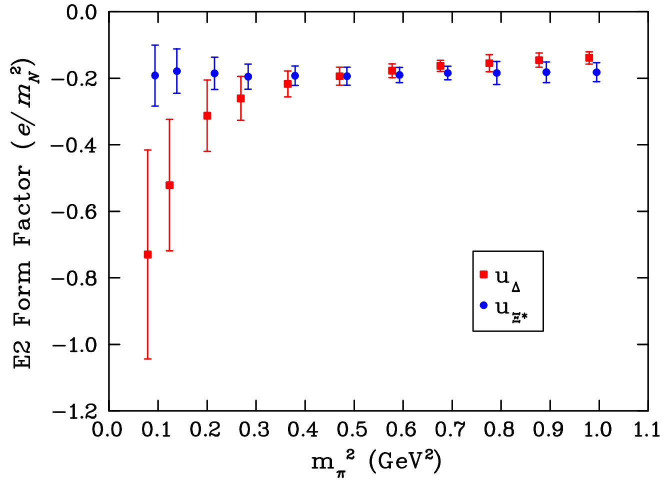

FIG. 31 (color online). *E*2 form factor contributions from the *u* quark sectors of the Δ and Ξ^*. The values for the Ξ^* are plotted at shifted m_π^2 for clarity.

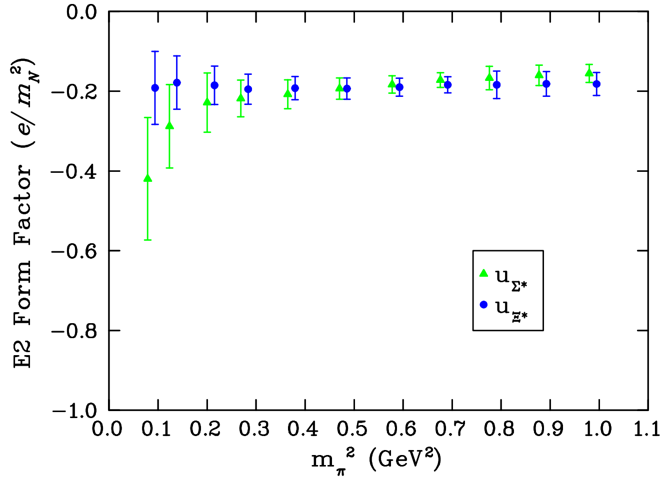

FIG. 32 (color online). *E*2 form factor contributions from the *u* quark sectors of the Σ^* and Ξ^*. The values for the Ξ^* are plotted at shifted m_π^2 for clarity.

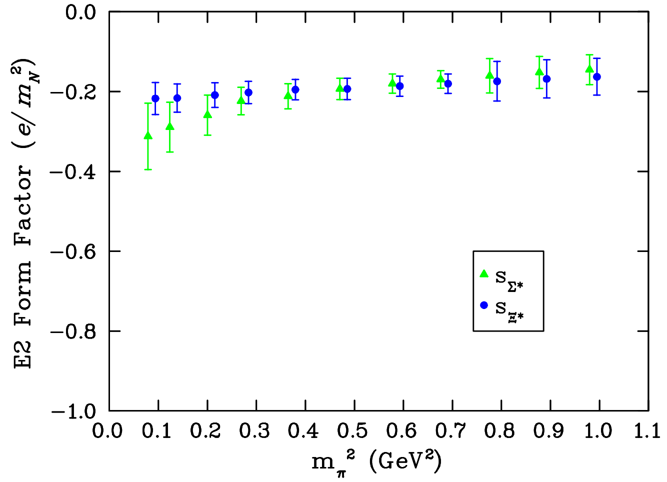

FIG. 33 (color online). *E*2 form factor contributions from the *s* quark sectors of the Σ^* and Ξ^*. The values for the Ξ^* are plotted at shifted m_π^2 for clarity.

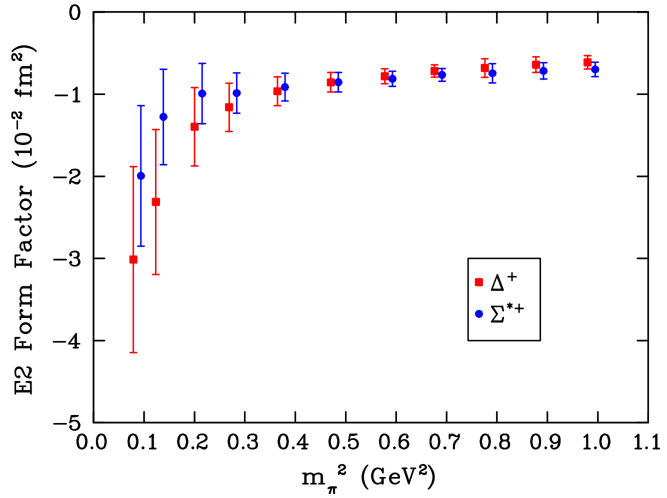

FIG. 34 (color online). Values of the *E*2 form factors in units of 10^{-2} fm^2 for the Δ^+ and Σ^{*+} at different quark masses. The values for Δ^+ are plotted at shifted m_π^2 for clarity.

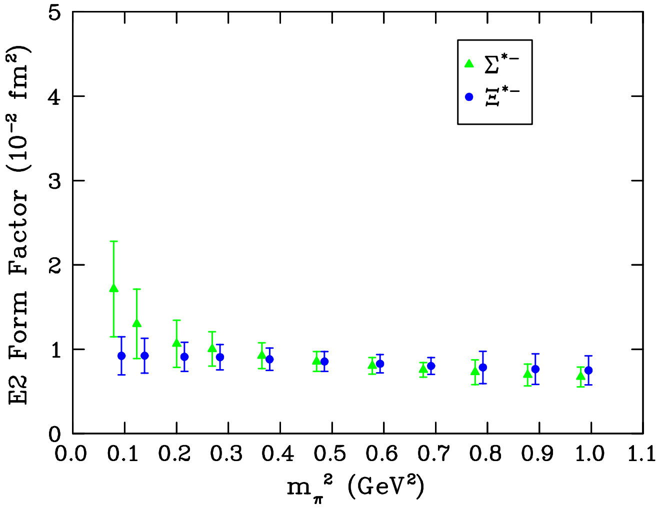

FIG. 35 (color online). $E2$ form factors in units of 10^{-2} fm^2 for the Σ^{*-} and Ξ^{*-} at different quark masses. The values for Σ^{*-} are plotted at shifted m_π^2 for clarity.

the $E2$ form factor of Ω^-, and we favor a positive value. Since Ω^- is a negatively charged baryon, this result implies that it has an oblate shape, with the equatorial axis being larger than the polar axis.

Similarly the $E2$ form factor for the Δ^+ is $(-0.86 \pm 0.12) \times 10^{-2}$ fm^2 at the $SU(3)$ flavor-symmetry point. Our results for the Δ^+ compare favorably with the results of Ref. [8]. Using the closest available pion masses of 533(3) and 563(4) MeV for this study, and [8] respectively, we find the $E2$ form factor to be $(-1.16 \pm 29) \times 10^{-2}$ fm^2, to be compared with $(-1.08 \pm 40) \times 10^{-2}$ fm^2. We note however, that this study is performed at a finite $Q^2 = 0.230(1)$ GeV^2, while [8] reports results at $Q^2 = 0$.

The negative $E2$ form factor of a positive Δ^+ baryon implies an oblate shape in the Breit frame. As illustrated in Fig. 34, the $E2$ form factor grows substantially in magnitude as the chiral limit is approached, taking the value $-0.030(11)$ fm^2 at our lightest quark mass. We note that the $E2$ form factor of Δ^{++} is twice that of the Δ^+ $E2$ form factor and hence takes the value $-0.060(23)$ fm^2 at our lightest quark mass.

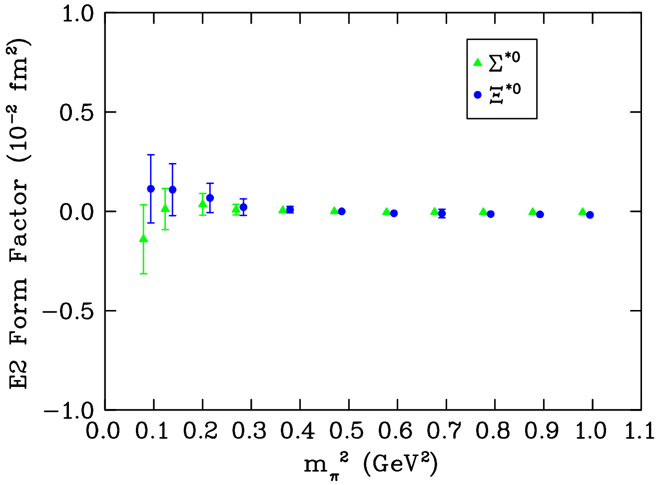

FIG. 36 (color online). $E2$ form factors in units of 10^{-2} fm^2 for the Σ^{*0} and Ξ^{*0} at different quark masses. The values for Σ^{*0} are plotted at shifted m_π^2 for clarity.

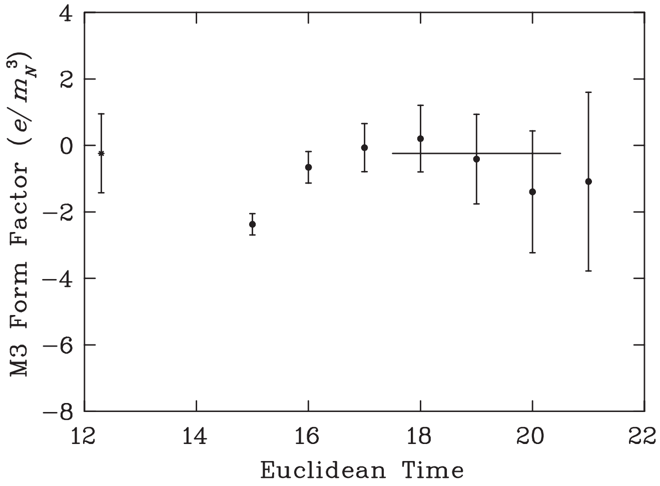

FIG. 37. $M3$ form factor of the Δ at the $SU(3)_{\text{flavor}}$ limit as a function of Euclidean time.

E. Magnetic-octupole moments

The magnetic-octupole form factors are calculated on the lattice by considering a combination of ratios of three- and two-point functions as given in Eq. (2.32).

Figure 37 provides a plot of the correlator proportional to the $M3$ form factor of a u quark in the Δ as a function of Euclidean time at the $SU(3)$ flavor limit. Figure 38 provides the $M3$ form factor at the ninth quark mass, where a plateau is realized using the splittings method. Tables XX,

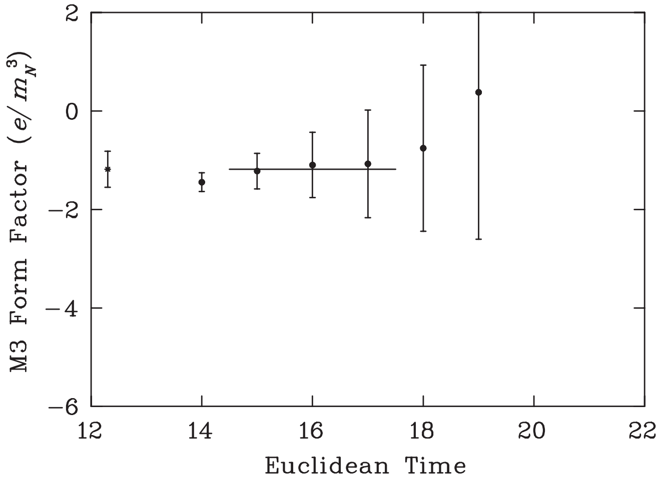

FIG. 38. $M3$ form factor (splitting) of the u quark sector of the Δ at the ninth quark mass where $m_\pi^2 = 0.215(4)$ GeV^2 as a function of time.

TABLE XX. Quark-sector contributions to the $M3$ form factor of Δ at $Q^2 = 0.230(1)$ GeV^2 in units of $e/2m_N^3$. Sector contributions are for a single quark having unit charge. The fit windows are selected using the criteria outlined in Ref. [14].

m_π^2 (GeV^2)		u_Δ			d_Δ	
	Fit value	Fit window	χ^2_{dof}	Fit value	Fit window	χ^2_{dof}
0.9972(55)	0.19(58)	18–22	0.83	0.19(58)	18–22	0.83
0.8936(56)	0.19(68)	18–22	0.63	0.19(68)	18–22	0.63
0.7920(55)	0.18(82)	18–22	0.50	0.18(82)	18–22	0.50
0.6920(54)	0.2(1.0)	18–22	0.44	0.2(1.0)	18–22	0.44
0.6910(35)	−0.10(75)	18–22	0.74	−0.10(75)	18–22	0.74
0.5925(33)	−0.09(87)	18–20	1.01	−0.09(87)	18–20	1.01
0.4854(31)	−0.2(1.2)	18–20	0.92	−0.2(1.2)	18–20	0.92
0.3795(31)	−0.4(1.4)	16–18	0.44	−0.4(1.4)	16–18	0.44
0.2839(33)	−0.8(1.6)	15–17	0.01	−0.8(1.6)	15–17	0.01
0.2153(35)	−1.2(1.9)	15–17	0.12	−1.2(1.9)	15–17	0.12
0.1384(43)	−2.4(2.5)	15–17	0.37	−2.4(2.5)	15–17	0.37
0.0939(44)	−3.7(3.3)	15–17	0.32	−3.7(3.3)	15–17	0.32

TABLE XXI. Quark-sector contributions to the $M3$ form factor of Σ^* baryons at $Q^2 = 0.230(1)$ GeV^2 in units of $e/2m_N^3$. Sector contributions are for a single quark having unit charge. The fit windows are selected using the criteria outlined in Ref. [14].

m_π^2 (GeV^2)		u_{Σ^*} or d_{Σ^*}			s_{Σ^*}	
	Fit value	Fit window	χ^2_{dof}	Fit value	Fit window	χ^2_{dof}
0.9972(55)	0.13(81)	18–22	0.56	0.64(80)	18–22	0.50
0.8936(56)	0.12(91)	18–22	0.50	0.63(90)	18–22	0.44
0.7920(55)	0.1(1.0)	18–22	0.48	0.6(1.0)	18–22	0.39
0.6920(54)	0.1(1.2)	18–22	0.47	0.6(1.2)	18–22	0.38
0.6910(35)	−0.16(89)	18–22	0.96	0.10(89)	18–22	0.64
0.5925(33)	−0.1(1.0)	18–20	1.03	−0.1(1.0)	18–20	0.90
0.4854(31)	−0.2(1.2)	18–20	0.92	−0.2(1.2)	18–20	0.92
0.3795(31)	−0.3(1.3)	16–18	0.43	−0.3(1.3)	16–18	0.61
0.2839(33)	−0.5(1.4)	15–17	0.01	−0.4(1.4)	15–17	0.30
0.2153(35)	−0.7(1.6)	15–17	0.01	−0.5(1.5)	15–17	0.38
0.1384(43)	−1.1(1.8)	15–17	0.21	−0.8(1.7)	15–17	0.07
0.0939(44)	−1.2(2.0)	15–17	0.07	−1.1(2.0)	15–17	0.89

TABLE XXII. Quark-sector contributions to the $M3$ form factor of Ξ^* baryons at $Q^2 = 0.230(1)$ GeV^2 in units of $e/2m_N^3$. Sector contributions are for a single quark having unit charge. The fit windows are selected using the criteria outlined in Ref. [14].

m_π^2 (GeV^2)		s_{Ξ^*}			u_{Ξ^*} or d_{Ξ^*}	
	Fit value	Fit window	χ^2_{dof}	Fit value	Fit window	χ^2_{dof}
0.9972(55)	0.6(1.1)	18–22	0.39	−0.1(1.2)	18–22	0.45
0.8936(56)	0.6(1.2)	18–22	0.39	−0.1(1.2)	18–22	0.48
0.7920(55)	0.5(1.3)	18–22	0.40	−0.1(1.3)	18–22	0.52
0.6920(54)	0.5(1.4)	18–22	0.41	0.0(1.4)	18–22	0.53
0.6910(35)	−0.2(1.1)	18–22	0.83	−0.3(1.1)	18–22	1.27
0.5925(33)	−0.2(1.1)	18–20	0.92	−0.2(1.1)	18–20	1.03
0.4854(31)	−0.2(1.2)	18–20	0.92	−0.2(1.2)	18–20	0.92
0.3795(31)	−0.3(1.2)	16–18	0.62	−0.3(1.2)	16–18	0.54
0.2839(33)	−0.3(1.3)	15–17	0.52	−0.4(1.3)	15–17	0.17
0.2153(35)	−0.3(1.3)	15–17	0.63	−0.4(1.4)	15–17	0.05
0.1384(43)	−0.3(1.4)	15–17	0.23	−0.6(1.4)	15–17	0.47
0.0939(44)	−0.4(1.4)	15–17	0.44	−0.3(1.5)	15–17	0.82

TABLE XXIII. $M3$ form factor results at $Q^2 = 0.230(1)$ GeV^2 of the charged decuplet baryons in units of $e/2m_N^3$ for different m_π^2 values. The $M3$ form factor of the Δ^- at the $SU(3)_{\text{flavor}}$ limit where $m_\pi^2 = 0.485(3)$ provides the $M3$ form factor of Ω^-.

m_π^2 (GeV^2)	Δ^{++}	Δ^+	Δ^-	Σ^{*+}	Σ^{*-}	Ξ^{*-}
0.9972(55)	0.4(1.2)	0.19(58)	−0.19(58)	−0.04(86)	−0.30(79)	−0.4(1.1)
0.8936(56)	0.4(1.4)	0.19(68)	−0.19(68)	−0.05(94)	−0.29(89)	−0.4(1.2)
0.7920(55)	0.4(1.6)	0.18(82)	−0.18(82)	−0.1(1.1)	−0.3(1.0)	−0.3(1.3)
0.6920(54)	0.4(2.0)	0.2(1.0)	−0.2(1.0)	−0.1(1.2)	−0.3(1.2)	−0.3(1.4)
0.6910(35)	−0.2(1.5)	−0.10(75)	0.10(75)	−0.18(90)	0.14(88)	0.2(1.1)
0.5925(33)	−0.2(1.7)	−0.09(87)	0.09(87)	−0.2(1.0)	0.1(1.0)	0.2(1.1)
0.4854(31)	−0.5(2.4)	−0.2(1.2)	0.2(1.2)	−0.2(1.2)	0.2(1.2)	0.2(1.2)
0.3795(31)	−0.8(2.8)	−0.4(1.4)	0.4(1.4)	−0.3(1.3)	0.3(1.3)	0.3(1.2)
0.2839(33)	−1.6(3.1)	−0.8(1.6)	0.8(1.6)	−0.6(1.4)	0.5(1.4)	0.3(1.3)
0.2153(35)	−2.4(3.8)	−1.2(1.9)	1.2(1.9)	−0.7(1.6)	0.6(1.5)	0.3(1.3)
0.1384(43)	−4.9(4.9)	−2.4(2.5)	2.4(2.5)	−1.2(1.9)	1.0(1.7)	0.4(1.4)
0.0939(44)	−7.4(6.6)	−3.7(3.3)	3.7(3.3)	−1.3(2.2)	1.2(1.9)	0.4(1.4)

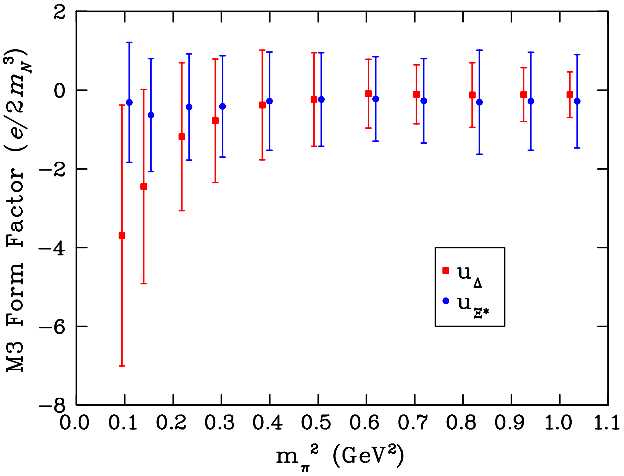

FIG. 39 (color online). $M3$ form factor contributions from the u quark sectors of the Δ and Ξ^*. The results for the Ξ^* are offset for clarity.

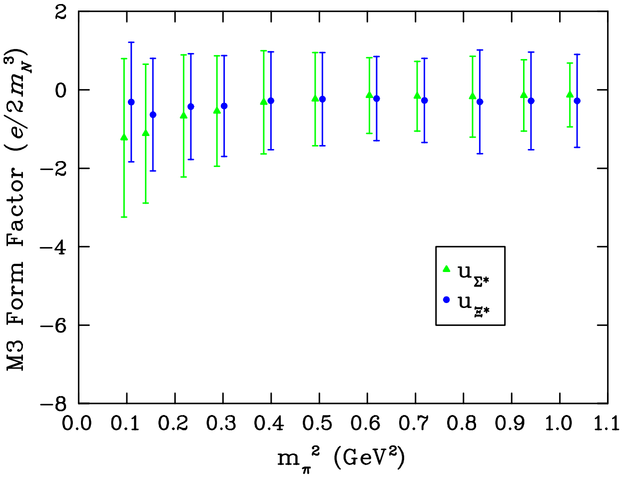

FIG. 40 (color online). $M3$ form factor contributions from the u quark sectors of the Σ^* and Ξ^*. The results for the Ξ^* have been offset for clarity.

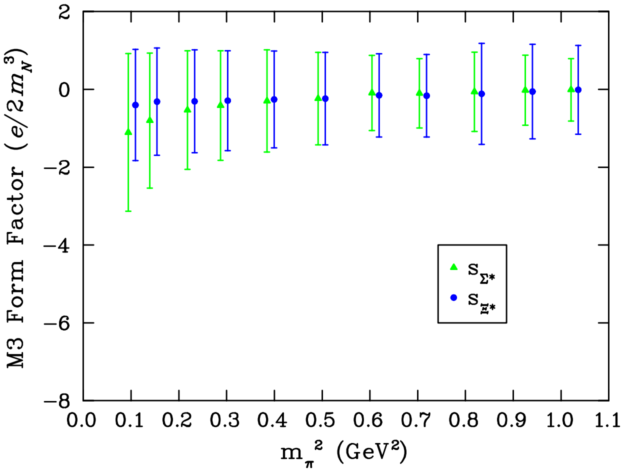

FIG. 41 (color online). $M3$ form factor contributions from the s quark sectors of the Σ^* and Ξ^*. The results for the Ξ^* have been offset for clarity.

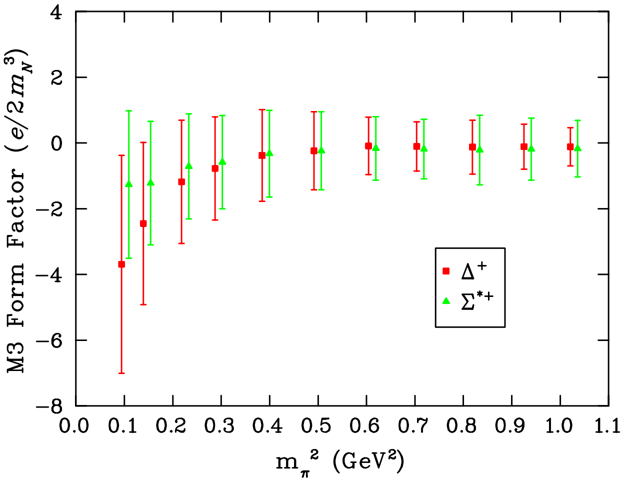

FIG. 42 (color online). $M3$ form factors for the Δ^+ and Σ^{*+} at different quark masses. The values for Σ^{*+} are plotted at shifted m_π^2 for clarity.

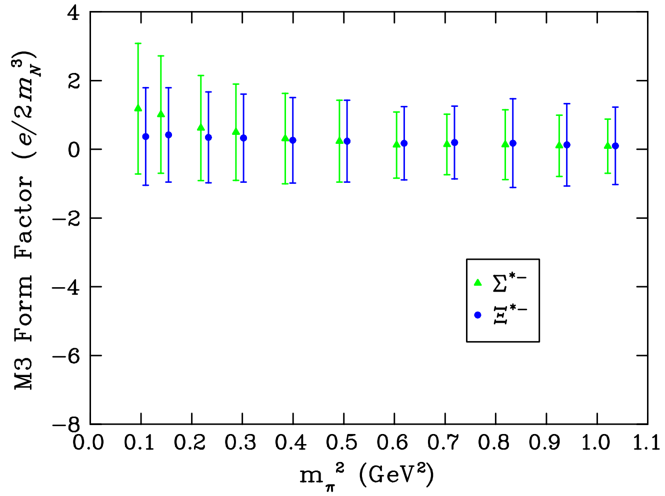

FIG. 43 (color online). $M3$ form factors for the Σ^{*-} and Ξ^{*-} at different quark masses. The values for Ξ^{*-} are plotted at shifted m_π^2 for clarity.

XXI, and XXII list the quark-sector $M3$ form factors. The magnetic-octupole form factors ($M3$) of the decuplet baryons are listed in Table XXIII.

Plots of the quark-sector contributions to the $M3$ form factors are provided in Figs. 39–41. Figures 42–44 show the $M3$ form factors for the decuplet baryons.

Like $E2$, the $M3$ form factors require nonzero orbital-angular momentum admixtures in the ground state wave function [7]. Our statistics are sufficient to reveal a nontrivial result for the $M3$ form factor of the Δ for the first time. We find a result of $-3.7(3.3)e/2m_N^3$ for the Δ^+ at a squared pion mass of 0.094(4) GeV^2, close to the physical limit. At larger masses the results are consistent with zero, but systematically negative, with enhancement at the lightest masses for the Δ, and to a lesser extent for the Σ^*.

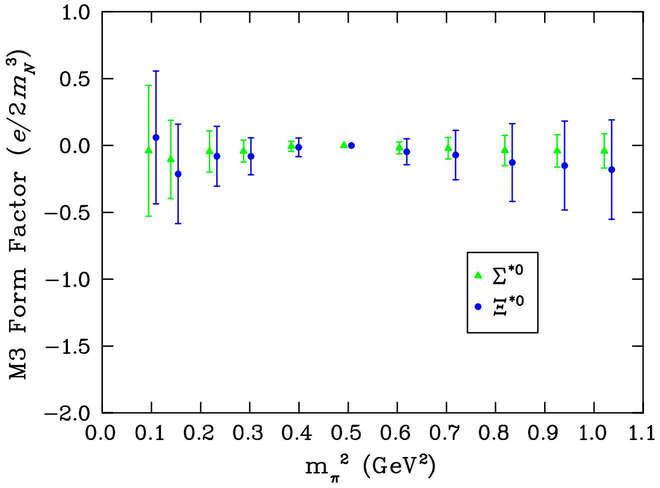

FIG. 44 (color online). $M3$ form factors for the Σ^{*0} and Ξ^{*0} at different quark masses. The values for Ξ^{*0} are plotted at shifted m_π^2 for clarity.

VI. SUMMARY

We have performed an extensive calculation of the electromagnetic properties of decuplet baryons at both the quark level and the baryon level, including the quadrupole and octupole form factors of the spin-3/2 baryons. For the first time we obtain nontrivial results for both the $E2$ and $M3$ form factors. In particular, we find decuplet baryons to be oblate in shape.

We find that the quarks in the decuplet are not as sensitive to their environment as their octet counterparts. Of particular note is the discovery that the decuplet-baryon radii are *smaller* than those of the octet baryons, contradicting the simple quark model, but substantiating hints in the early study of Ref. [7].

A particularly interesting finding is that the suppression of sea-quark loop contributions in quenched QCD reduces the decuplet magnetic moment considerably, resulting in a turnover in the magnetic moment at the lighter quark masses, as illustrated in Fig. 27. At large pion masses, the Δ^+ moment is enhanced relative to the proton moment in accord with earlier quenched lattice QCD calculations [7,23] and model expectations. However, as the chiral regime is approached, the nonanalytic behavior of the quenched meson cloud starts to be revealed, enhancing the proton and suppressing the Δ^+, in accord with the expectations of QχPT. This suppression should be absent in full QCD. Hence this is one particular case that we have identified as a place to look for effects of unquenching in future dynamical simulations. We also predict that unquenching effects should be observed in the Ω^- magnetic moment, which we find to be suppressed in quenched QCD with regard to the experimentally measured value due to the absence of $K\Xi$ loops in the virtual decay of Ω^-. We also expect that future studies nearer the chiral limit will support the initial results observed in this study. In this case however, it will be important to consider multiple lattice volumes in order to quantify the volume dependence of results near the chiral limit.

Through a calculation of the decuplet $E2$ form factors and electric-quadrupole moments, we predict oblate shapes for the decuplet baryons. It will be interesting to confront this prediction with an experimental measurement of the Ω^- quadrupole form factor. We provide a summary of all the Ω^- measurements in Table XXIV.

TABLE XXIV. Collected results for the Ω^-. Results are obtained from the Δ^- at the $SU(3)_{\text{flavor}}$ limit, where $m_\pi^2 = 0.4854(31)$ GeV^2.

Quantity	Fit value
Mass (GeV)	1.732(12)
Charge radius (fm^2)	−0.307(15)
Magnetic moment (μ_N)	−1.697(65)
$E2$ form factor (10^{-2} fm^2)	0.86(12)
$M3$ form factor ($e/2m_N^3$)	0.2(1.2)

Finally we have obtained nontrivial values for the $M3$ form factor for the first time in lattice QCD studies. These results provide an interesting and novel forum for the further development of our understanding of nonperturbative QCD.

ACKNOWLEDGMENTS

We thank the Australian Partnership for Advanced Computing (APAC) and the South Australian Partnership for Advanced Computing (SAPAC) for generous grants of supercomputer time which have enabled this project. This work was supported by the Australian Research Council. J. Z. is supported by STFC Grant No. PP/F009658/1. J. B. Z. is supported by Chinese NSFC Grants No. 10675101 and No. 10835002.

---

[1] J. Arrington, C. D. Roberts, and J. M. Zanotti, J. Phys. G **34**, S23 (2007).
[2] K. de Jager, AIP Conf. Proc. **904**, 95 (2007).
[3] H. y. Gao, Int. J. Mod. Phys. E **12**, 1 (2003); **12**, 567(E) (2003).
[4] C. E. Hyde-Wright and K. de Jager, Annu. Rev. Nucl. Part. Sci. **54**, 217 (2004).
[5] C. F. Perdrisat, V. Punjabi, and M. Vanderhaeghen, Prog. Part. Nucl. Phys. **59**, 694 (2007).
[6] J. M. Zanotti, PoS, LAT2008 (2008) 007 [arXiv:0812.3845].
[7] D. B. Leinweber, T. Draper, and R. M. Woloshyn, Phys. Rev. D **46**, 3067 (1992).
[8] C. Alexandrou, T. Korzec, T. Leontiou, J. W. Negele, and A. Tsapalis, PoS, LAT2007 (2007) 149 [arXiv:0710.2744].
[9] C. Alexandrou *et al.*, Phys. Rev. D **79**, 014507 (2009).
[10] D. B. Leinweber *et al.*, Phys. Rev. Lett. **94**, 212001 (2005).
[11] D. B. Leinweber *et al.*, Phys. Rev. Lett. **97**, 022001 (2006).
[12] R. D. Young, J. Roche, R. D. Carlini, and A. W. Thomas, Phys. Rev. Lett. **97**, 102002 (2006).
[13] A. Acha *et al.* (HAPPEX Collaboration), Phys. Rev. Lett. **98**, 032301 (2007).
[14] S. Boinepalli, D. B. Leinweber, A. G. Williams, J. M. Zanotti, and J. B. Zhang, Phys. Rev. D **74**, 093005 (2006).
[15] J. N. Hedditch, W. Kamleh, B. G. Lasscock, D. B. Leinweber, A. G. Williams, and J. M. Zanotti, Phys. Rev. D **75**, 094504 (2007).
[16] B. L. Ioffe, Nucl. Phys. **B188**, 317 (1981); **B191**, 591(E) (1981).
[17] Y. Chung, H. G. Dosch, M. Kremer, and D. Schall, Nucl. Phys. **B197**, 55 (1982).
[18] J. J. Sakurai, *Advanced Quantum Mechanics* (Addison-Wesley, Reading, MA, 1982).
[19] Y. Kuramashi, M. Fukugita, H. Mino, M. Okawa, and A. Ukawa, Phys. Rev. Lett. **71**, 2387 (1993).
[20] S. J. Dong and K. F. Liu, Phys. Lett. B **328**, 130 (1994).
[21] M. Benmerrouche, R. M. Davidson, and N. C. Mukhopadhyay, Phys. Rev. C **39**, 2339 (1989).
[22] S. Nozawa and D. B. Leinweber, Phys. Rev. D **42**, 3567 (1990).
[23] D. B. Leinweber, R. M. Woloshyn, and T. Draper, Phys. Rev. D **43**, 1659 (1991).
[24] W. Wilcox, T. Draper, and K. F. Liu, Phys. Rev. D **46**, 1109 (1992).
[25] M. Luscher and P. Weisz, Commun. Math. Phys. **97**, 59 (1985); **98**, 433 (1985).
[26] R. Sommer, Nucl. Phys. **B411**, 839 (1994).
[27] J. M. Zanotti *et al.* (CSSM Lattice Collaboration), Phys. Rev. D **65**, 074507 (2002).
[28] J. M. Zanotti, B. Lasscock, D. B. Leinweber, and A. G. Williams, Phys. Rev. D **71**, 034510 (2005).
[29] S. Boinepalli, W. Kamleh, D. B. Leinweber, A. G. Williams, and J. M. Zanotti, Phys. Lett. B **616**, 196 (2005).
[30] W. Kamleh, D. B. Leinweber, and A. G. Williams, Phys. Rev. D **70**, 014502 (2004).
[31] R. D. Young, D. B. Leinweber, A. W. Thomas, and S. W. Wright, Phys. Rev. D **66**, 094507 (2002).
[32] J. N. Labrenz and S. R. Sharpe, Phys. Rev. D **54**, 4595 (1996).
[33] D. B. Leinweber *et al.*, Eur. Phys. J. C **18**, 247 (2003).
[34] M. Gockeler *et al.* (QCDSF Collaboration), Phys. Rev. D **71**, 034508 (2005).
[35] D. B. Leinweber, Phys. Rev. D **47**, 5096 (1993).
[36] I. C. Cloet, D. B. Leinweber, and A. W. Thomas, Phys. Lett. B **563**, 157 (2003).
[37] D. B. Leinweber, A. W. Thomas, A. G. Williams, R. D. Young, J. M. Zanotti, and J. B. Zhang, Nucl. Phys. **A737**, 177 (2004).